NeuroImage 295 (2024) 120658

Contents lists available at ScienceDirect

NeuroImage

journal homepage: www.elsevier.com/locate/ynimg

Synaptic signaling modeled by functional connectivity predicts metabolic demands of the human brain

Sebastian Klug [a,b], Matej Murgaš [a,b], Godber M Godbersen [a,b], Marcus Hacker [c], Rupert Lanzenberger [a,b], Andreas Hahn [a,b,*], For the Alzheimer's Disease Neuroimaging Initiative[1]

[a] Department of Psychiatry and Psychotherapy, Medical University of Vienna, Austria
[b] Comprehensive Center for Clinical Neurosciences and Mental Health (C3NMH), Medical University of Vienna, Austria
[c] Department of Biomedical Imaging and Image-guided Therapy, Division of Nuclear Medicine, Medical University of Vienna, Austria

ARTICLE INFO

Keywords:
Simultaneous PET/MRI
Brain metabolism
Functional PET
Functional connectivity
Metabolic connectivity mapping

ABSTRACT

Purpose: The human brain is characterized by interacting large-scale functional networks fueled by glucose metabolism. Since former studies could not sufficiently clarify how these functional connections shape glucose metabolism, we aimed to provide a neurophysiologically-based approach.
Methods: 51 healthy volunteers underwent simultaneous PET/MRI to obtain BOLD functional connectivity and [^{18}F]FDG glucose metabolism. These multimodal imaging proxies of fMRI and PET were combined in a whole-brain extension of metabolic connectivity mapping. Specifically, functional connectivity of all brain regions were used as input to explain glucose metabolism of a given target region. This enabled the modeling of postsynaptic energy demands by incoming signals from distinct brain regions.
Results: Functional connectivity input explained a substantial part of metabolic demands but with pronounced regional variations (34 - 76%). During cognitive task performance this multimodal association revealed a shift to higher network integration compared to resting state. In healthy aging, a dedifferentiation (decreased segregated/modular structure of the brain) of brain networks during rest was observed. Furthermore, by including data from mRNA maps, [^{11}C]UCB-J synaptic density and aerobic glycolysis (oxygen-to-glucose index from PET data), we show that whole-brain functional input reflects non-oxidative, on-demand metabolism of synaptic signaling. The metabolically-derived directionality of functional inputs further marked them as top-down predictions. In addition, the approach uncovered formerly hidden networks with superior efficiency through metabolically informed network partitioning.
Conclusions: Applying multimodal imaging, we decipher a crucial part of the metabolic and neurophysiological basis of functional connections in the brain as interregional on-demand synaptic signaling fueled by anaerobic metabolism. The observed task- and age-related effects indicate promising future applications to characterize human brain function and clinical alterations.

1. Introduction

Human brain function is organized by the coordinated activity of different brain regions, composing large-scale functional networks. These may flexibly reconfigure between rest and task states (Hearne et al., 2017), while this ability is altered with aging (Wig, 2017). Network interactions are primarily characterized by functional connectivity (FC), correlating the time course of the hemodynamic response of different brain regions as obtained via BOLD fMRI (Yeo et al., 2011). Despite the advancement of our understanding of human brain function through BOLD imaging, its underlying physiology marks it as a mixed, semiquantitative signal of cerebrovascular sources and neuronal activity

* Corresponding author at: Medical University of Vienna, Austria, Waehringer Guertel 18-20, 1090 Vienna, Austria.
E-mail address: andreas.hahn@meduniwien.ac.at (A. Hahn).

[1] Data used in preparation of this article were obtained from the Alzheimer's Disease Neuroimaging Initiative (ADNI) database (adni.loni.usc.edu). As such, the investigators within the ADNI contributed to the design and implementation of ADNI and/or provided data but did not participate in analysis or writing of this report. A complete listing of ADNI investigators can be found at: http://adni.loni.usc.edu/wp-content/uploads/how_to_apply/ADNI_Acknowledgement_List.pdf

https://doi.org/10.1016/j.neuroimage.2024.120658
Received 15 January 2024; Received in revised form 22 April 2024; Accepted 27 May 2024
Available online 28 May 2024

(Hillman, 2014; Logothetis, 2008). Recent multimodal approaches with simultaneous [^{18}F]FDG PET acquisition of comparable temporal resolution (so-called functional PET (fPET)) (Hahn et al., 2018, 2016; Jamadar et al., 2019; Rischka et al., 2018; Villien et al., 2014) enable an indirect dynamic assessment of neuronal activation via the cerebral metabolic rate of glucose (CMRGlu), capturing a fully quantitative molecular marker of primarily synaptic activity (Magistretti and Allaman, 2015; Sokoloff, 1981; Sokoloff et al., 1977), which is largely unaffected by blood flow (Leybaert, 2005).

Several previous studies already investigated the relationship between FC and CMRGlu, overall indicating a relationship between the number or strength of functional connections of a region and its metabolic demands. However, these approaches were limited by the assessment of regional connectivity surrogates (such as ReHo, fALFF, or connectivity density/strength) and/or subsequent associations across the entire brain (Aiello et al., 2015; Nugent et al., 2015; Palombit et al., 2022; Shokri-Kojori et al., 2019; Tomasi et al., 2013, 2017). Even a sophisticated combination of 50 BOLD- and FC-derived features only explained up to 40% of the CMRGlu variance (Volpi et al., 2021). Thus, it appears that the above-mentioned regional summary metrics of FC do not sufficiently reflect the underlying metabolic demands, potentially due to the loss of information that is inherent to averaging within a region (mathematically, a $1\times k$ summary vector is derived from a $k\times k$ FC matrix to enable correlation with a $1\times k$ CMRGlu vector). In contrast, few studies examined associations between a region's metabolism and FC with specific remote brain regions (Riedl et al., 2014). Such a strategy may be more informative under the hypothesis that FC input leads to increased glucose metabolism in a certain brain region.

This approach has been elegantly formulated in the framework of metabolic connectivity mapping (MCM) (Riedl et al., 2016), which rests upon physiological observations on the interaction of the BOLD signal and glucose metabolism. These are both driven by glutamate release upon neuronal activation, which in turn leads to increases in cerebral blood flow through neurovascular coupling (Attwell et al., 2010; Mishra et al., 2016) and glucose uptake in neurons (Lundgaard et al., 2015) and astrocytes (Zimmer et al., 2017). The fact that in gray matter, about 70% of energy is consumed postsynaptically (Attwell and Laughlin, 2001; Harris et al., 2012; Mergenthaler et al., 2013; Yu et al., 2018) implies that incoming signals from other brain regions play an essential role in the resulting metabolism of a target area. This also enables to identify the target region and thus infer the directionality of a connection. Specifically, if the evoked connectivity pattern in the target region is causally related to the seed region, this will be reflected in a spatially correlated CMRGlu pattern in the target (Hahn et al., 2020; Riedl et al., 2016). This spatial correlation between CMRGlu and FC patterns as calculated by MCM has already proven feasible in characterizing hierarchical interactions of the brain during rest and task performance (Hahn et al., 2020; Riedl et al., 2016) and their adaptations after learning a visuospatial task (Klug et al., 2022). It has also been validated with dynamic causal modeling (DCM) (Hahn et al., 2020). More specifically, Bayesian model comparison within the framework of DCM indicated that the most plausible model of directed connectivity between task-related brain regions converged with the model identified via MCM. Using family-wise inference to test each connection's relevance individually proved this result's specificity (Hahn et al., 2020).

In this work, we leverage MCM from pairwise regional interactions to a whole-brain model, aiming to identify the proportion of BOLD FC that represents postsynaptic metabolic demands. We thereby investigate each brain region's FC as a potential input signal to a given target region and compute the maximum amount of explained CMRGlu independently for each region and individual. We investigated potential differences between rest and task states as well as between young and elderly subjects. Following recent studies showing differences in this association (Palombit et al., 2022; Volpi et al., 2021), we expect region- and network-specific variations in the ability of FC to predict CMRGlu. Focusing on the prominent role of synaptic processes in brain energy demands, we hypothesize that the associations between FC and CMRGlu are reflected in the corresponding gene expression patterns, synaptic density as well as aerobic glycolysis (AG). AG is a proxy of non-oxidative energy demands, which is related to synaptic plasticity (amongst others) (Goyal et al., 2014) and changes its pattern with aging (Goyal et al., 2017). Throughout our work, we aim to clarify the interrelation of two of the most prominent noninvasive proxies of neuronal activation in the human brain, namely BOLD fMRI and [^{18}F]FDG PET.

2. Material and methods

This work combined [^{18}F]FDG fPET and blood-oxygen level dependent (BOLD) fMRI data from 51 healthy participants. The two imaging modalities were acquired simultaneously at resting state and during the performance of a cognitive task (the video game Tetris®), which requires rapid visuospatial processing and motor coordination (Hahn et al., 2020; Klug et al., 2022).

The obtained glucose metabolism (CMRGlu) and functional connectivity (FC) were modeled in the framework of metabolic connectivity mapping (MCM, see above) (Hahn et al., 2020; Klug et al., 2022; Riedl et al., 2016). We extended the MCM framework by computing spatial correlations not only for FC with a single brain region but for FC patterns elicited in the target region by the entire brain while controlling for collinearity between different FC inputs as well as randomly explained variance in CMRGlu (Fig. 1). This enabled us to assess for each participant and brain region the maximum amount of CMRGlu explained by FC. To relate these observations with the underlying neurophysiological processes, the resulting spatial distribution of explained CMRGlu was compared to that of mRNA expressions (Diez and Sepulcre, 2018) as well as synaptic density obtained from [^{11}C]UCB-J PET (Rossano et al., 2020) and the oxygen-to-glucose index (OGI) as a metric of aerobic glycolysis (Goyal et al., 2023). We further investigated alterations of explained metabolic demands during task performance and in healthy aging, the latter with data from the Alzheimer's Disease Neuroimaging Initative 2 (ADNI 2) cohort. This was followed by a detailed assessment of within and between network contributions to explain CMRGlu in the different conditions and cohorts. Finally, the additional value of incorporating metabolic information for the refinement of functional brain network organization was evaluated.

For the young adult cohort, the experimental design, cognitive task, PET/MR data acquisition, blood sampling, and data preprocessing have been described in full detail in our previous work (Hahn et al., 2020; Klug et al., 2022). Hence, these aspects will only be covered briefly here. For the ADNI 2 cohort, all processing steps were identical if not specified otherwise.

Data used in the preparation of this article were obtained from the Alzheimer's Disease Neuroimaging Initiative (ADNI) database (adni.loni.usc.edu). The ADNI was launched in 2003 as a public-private partnership, led by Principal Investigator Michael W. Weiner, MD. The primary goal of ADNI has been to test whether serial magnetic resonance imaging (MRI), positron emission tomography (PET), other biological markers, and clinical and neuropsychological assessment can be combined to measure the progression of mild cognitive impairment (MCI) and early Alzheimer's disease (AD).

2.1. Experimental design

Young adult participants underwent a simultaneous PET/MRI scan while performing a cognitive task (the video game Tetris®). First, structural (8 min) and BOLD fMRI (6 min) were acquired at the resting state. This was followed by fPET (52 min) using the radiotracer [^{18}F]FDG. After an initial period of rest (8 min), the cognitive task was performed in two levels of difficulty (2 easy and 2 hard conditions in randomized order, 6 min continuous performance each, 5 min rest after each task). During the task, BOLD fMRI was also recorded. fPET data was used for the quantification of CMRGlu, and BOLD fMRI served for the

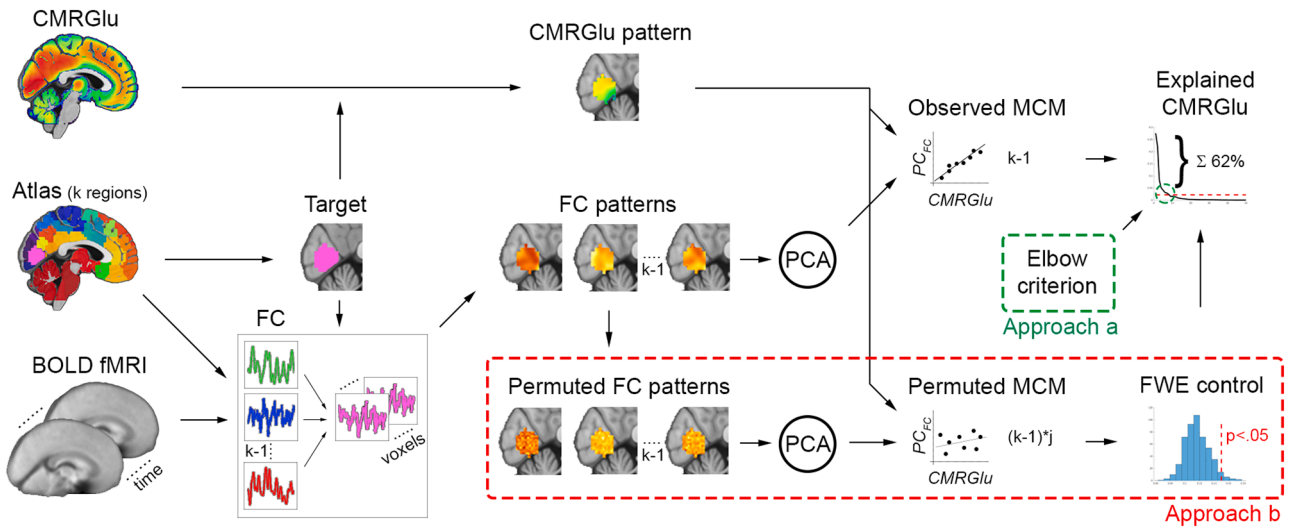

Fig. 1. *Schematic algorithm overview, extending metabolic connectivity mapping (MCM) to a whole-brain model to explain glucose metabolism (CMRGlu) by functional connectivity (FC).* A target region (magenta) is selected from an atlas with k regions. FC between the target and all other brain regions is then computed from the BOLD signal time series, yielding k-1 voxel-wise FC patterns in the target. To remove collinearity among the FC target patterns, principal component analysis (PCA) is applied. The obtained k-1 orthogonal principal components of FC patterns (PC_{FC}, i.e., linear combinations of FC patterns) are spatially correlated with the corresponding voxel-wise CMRGlu pattern of the target, resulting in k-1 observed MCM correlation values. Two different approaches were used to assess which correlations are significantly higher than random. Approach a employs the elbow criterion (i.e., identifying the point with minimum distance to the origin), providing a computationally fast method to estimate the total amount of explained CMRGlu by PC_{FC} in the target region as r^2. In approach b, each FC target pattern was randomly permuted across voxels, subject to PCA, and again correlated with the PC_{FC} patterns of the target. Repeating the permutation process j times results in (k-1)*j random MCM correlation values. For each permutation, the maximum value across all k-1 correlations was selected to build a random distribution. Using the top 5% of permuted MCM values as a cutoff has robust control for type-I statistical errors at $p < 0.05$ FWE-corrected (Genovese et al., 2002; Holmes et al., 1996). These procedures are repeated k times, assigning a different region as a target each time to obtain whole-brain estimates of explained CMRGlu.

computation of functional connectivity. For all periods of rest, participants had their eyes open, looked at a cross-hair, relaxed, and were instructed not to focus on anything in particular.

Participants of the ADNI 2 cohort underwent separate sessions of structural and BOLD fMRI as well as [^{18}F]FDG PET.

2.2. Cognitive task

We employed an adapted version of the video game Tetris® (https://github.com/jakesgordon/javascript-tetris, MIT license) as implemented in electron 1.3.14. Participants are required to build complete horizontal lines by aligning bricks, which descend from the top of the screen. The easy and hard levels of difficulty varied with respect to the speed of the descending bricks (1 and 3 lines per sec) and the number of incomplete lines already built at the bottom of the screen (2 and 6 lines out of 20). A practice run was carried out right before the start of the scan (30 s for each level of difficulty) to enable participants to familiarize themselves with the control buttons. The paradigm is cognitively challenging and requires among other skills rapid visuo-spatial motor coordination, mental rotation and a high level of attention.

Data of the ADNI 2 cohort were acquired at resting-state.

2.3. Participants

For this study, 53 healthy young adults were initially recruited, and 51 were included (mean age ± sd = 23.3 ± 3.3 years, 24 female). Two participants were excluded due to failure of arterial blood sampling and excessive head motion during the BOLD acquisition (31.2% of frames required scrubbing, see rsfMRI preprocessing). Parts of these data were already included in our previous work (Godbersen et al., 2023; Hahn et al., 2020; Klug et al., 2022; Rischka et al., 2021). Recent studies with MCM showed robust estimation of directional connectivity with sample sizes of 22 and 24 subjects. As the current study sample is more than two times larger, a formal sample size estimation was omitted. An initial screening visit was conducted to ensure general health with a routine medical examination (blood tests, electrocardiogram, neurological testing, structured clinical interview for DSM-IV). Female participants completed a urine pregnancy test at the screening visit and before the PET/MRI scan. Exclusion criteria were current or previous somatic, neurological, or psychiatric disorders (within the last 12 months), substance abuse or psychopharmacological medication (6 months), current pregnancy or breastfeeding, contraindications for MRI examination, previous study-related radiation exposure (10 years) and experience with the video game Tetris® (3 years). After a detailed explanation of the study, all participants provided written informed consent, they were insured and reimbursed for participation. This study was approved by the Ethics Committee of the Medical University of Vienna (ethics number 1479/2015), and procedures were carried out according to the Declaration of Helsinki. The study was pre-registered at ClinicalTrials.gov (NCT03485066).

The initial sample of the ADNI 2 cohort used in this work comprised 47 healthy elderly subjects, as only for those three data sets were available (T1-weighted MRI, resting-state BOLD fMRI and [^{18}F]FDG PET). Six subjects were excluded due to excessive head motion during the BOLD sequence ($n = 4$, more than 80% of frames required scrubbing, see rsfMRI preprocessing), different BOLD acquisition parameters ($n = 1$) and questionable quality of PET data ($n = 1$). Thus, the final sample of healthy elderly comprised 41 participants (76.6 ± 7.0 years, 21 female).

2.4. PET/MR data acquisition

Except for unsweetened water, participants fasted for at least 5.5 h before the start of the PET/MRI examination (Guedj et al., 2022). The radiotracer [^{18}F]FDG was administered intravenously as a bolus (510 kBq/kg for 1 min) plus constant infusion (40 kBq/kg for 51 min). The perfusion pump for the administration (Syramed μSP6000, Arcomed, Regensdorf, Switzerland) was kept in an MRI shield (UniQUE, Arcomed). MRI acquisition comprised a T1-weighted MPRAGE sequence (TE = 4.21 ms, TR = 2200 ms, TI = 900 ms, flip angle = 9°, voxel size = 1 × 1 × 1 mm + 0.1 mm gap, 7.72 min) and BOLD fMRI for functional

connectivity using an EPI sequence (TE = 30 ms, TR = 2000 ms, flip angle = 90°, voxel size = 2.5 × 2.5 × 2.5 mm + 0.825 mm gap, 6 min for each condition).

For the ADNI 2 cohort, similar MRI raw data was available with a T1-weighted MPRAGE sequence (TE = 3.16 ms, TR = 6800 ms, TI = 0 ms, flip angle = 9°, voxel size = 1.2 × 1 × 1 mm) and BOLD fMRI at resting state (TE = 30 ms, TR = 3000 ms, flip angle = 80°, voxel size = 3.3125×3.3125×3.313 mm, 7 min). For this cohort, [^{18}F]FDG was administered as a single bolus and raw data comprised 6 frames.

2.5. Blood sampling

Before the PET/MRI scan, blood glucose levels were determined as triplicate. During the scan, manual arterial samples were collected approx. at 3, 4, 5, 14, 25, 36 and 47 min after the start of the radiotracer administration. Whole-blood activity and, after centrifugation, plasma activity were measured in a gamma counter (Wizard2, Perkin Elmer). The arterial input function was obtained by multiplication of the average plasma-to-whole-blood ratio with whole-blood data.

For ADNI 2 data, no blood samples were available.

2.6. Quantification of glucose metabolism & determination of amyloid status

fPET data were corrected for attenuation (Burgos et al., 2014) and reconstructed to frames of 30 s. Preprocessing was carried out in SPM12 (https://www.fil.ion.ucl.ac.uk/spm/) with motion correction, spatial normalization to MNI space via the T1-weighted image (final voxel size 2 × 2 × 2 mm), and smoothing with a Gaussian kernel of 8 mm. Non-gray matter voxels were excluded and a low-pass filter was applied. Baseline metabolism and task-specific effects were separated with the general linear model (GLM). Regressors included baseline metabolism (average gray matter signal excluding voxel active during the hard task), the two task conditions (linear ramp function), and head motion (the first principal component of motion parameters). The Patlak plot was used for absolute quantification of the net influx constant K_i, which was converted to the cerebral metabolic rate of glucose (CMRGlu). This yields separate maps of baseline and task-induced CMRGlu, which were then used for the computation of MCM (see below).

For the ADNI 2 cohort, preprocessing included motion correction, temporal averaging across the 6 time frames, and spatial normalization via the T1-weighted image in SPM12 (final voxel size of 2 × 2 × 2 mm) and smoothing with a Gaussian kernel of 8 mm. Standard uptake value ratios (SUVR) were then calculated using whole brain gray matter as a reference. PET data were not corrected for partial volume effects (except OGI, see below).

To assess amyloid accumulation in the ADNI 2 cohort, [^{18}F]AV-45 florbetapir scans were downloaded from the ADNI database (39 of 41 subjects with available scans). Processing of florbetapir scans was done in accordance with [^{18}F]FDG scans (i.e., motion correction, temporal averaging, spatial normalization via T1-weighted image). Amyloid status was determined according to published procedures (Farrell et al., 2021; Mormino, 2014). Briefly, SUVR was calculated across large cortical regions using the Desikan-Killiany Mindboggle atlas (Klein and Tourville, 2012) (frontal, cingulate, parietal, lateral temporal) with reference to the whole cerebellum. Previous work also recommended thresholds to assign amyloid positivity using Gaussian mixture modeling as SUVR = 1.126 (Mormino, 2014) or 1.09 (Farrell et al., 2021).

2.7. rsfMRI preprocessing

fMRI data were preprocessed using SPM12 as described previously (Hahn et al., 2020). This included correction for slice timing effects (reference = middle slice) and motion (quality = 1, register to mean option), followed by spatial normalization to MNI space via the T1-weighted image (final voxel size = 2 × 2 × 2 mm) and smoothing with a Gaussian kernel of 8 mm.

To avoid influence of motion artifacts, motion scrubbing was applied (Power et al., 2015). Frame-wise displacement was calculated from the six realignment parameters. For rotation parameters, degrees were converted to millimeters as the displacement on the surface of a sphere with radius = 50 mm. Frames with framewise displacement > 0.5 mm were removed from the analysis (plus one frame back and two forward). Average framewise displacement in young healthy adults was 0.19 ± 0.11 mm (before removal of frames).

To minimize the influence of potentially confounding signals, linear regression was applied (realignment parameters, signals from white matter and cerebrospinal fluid), followed by band-pass filtering. To enable comparison of functional connectivity between resting-state and task performance, cutoff frequencies were set to 0.01 < 0.15 Hz (Sun et al., 2004).

For the ADNI 2 cohort, preprocessing of fMRI data was identical, except that the limit for removal of frames was framewise displacement = 1 mm. Average framewise displacement (before removal of frames) in the elderly cohort was 0.42 ± 0.15 mm.

2.8. Region of interest atlas & network parcellation

To avoid dependency of the results based on a specific brain parcellation, several different parcellation schemes and atlases were used (Suppl. Fig. S2). The Craddock atlas with 200 parcels was used (Craddock et al., 2012) as it has several advantages for the employed MCM approach. 1) It covers the entire brain, including subcortical regions and the cerebellum. 2) Parcels are related to functional instead of structural characteristics. 3) Parcels are represented by entire volumes instead of discrete MNI coordinates, with relatively slight volumetric variation (average region size = 91.9 ± 18.8 mm^3). In addition, the version with 100 and 400 parcels was used. Furthermore, the Schaefer atlas with 200 cortical parcels was used (Schaefer et al., 2018), and FreeSurfer regions were added for the subcortex and cerebellum (Fischl et al., 2002). We applied a previously described 7-network parcellation that was initially assessed on one thousand subjects (Yeo et al., 2011). This parcellation comprises the Visual network (VI), the Somatomotor Network (SM), the Dorsal Attention Network (DA), the Ventral Attention Network (VA), the Frontoparietal Network (FP), the Default Mode Network (DM) and the Limbic Network/Frontotemporal Network (FT in our data). This parcellation scheme was extended by the Hippocampus/Amygdala (HI), the Basal Ganglia (BG: Striatum & Thalamus) and the Cerebellum (CE, all from Harvard Oxford Atlas as provided in FSL) to also cover subcortical regions.

2.9. Whole-brain MCM model

We extended the framework of MCM from the interaction between two brain regions to a whole-brain approach (Fig. 1, Suppl. Fig. 1). In its original implementation, MCM was calculated as the spatial correlation between the FC pattern that one source region elicits in a target region with this target region's metabolic pattern, as assessed by SUVR (Standardized Uptake Value Ratio; reference to whole brain uptake) of [^{18}F]FDG PET (Riedl et al., 2016). In contrast, we aim to explain regional metabolic demands by all of its input signals, which are, in turn, represented by the functional connectivity of the entire brain. The herein employed whole-brain approach uses all non-target (k-1) brain regions as the functional input to the target region and spatially correlates the resulting FC pattern with the CMRGlu pattern as assessed by functional PET. For the different [^{18}F]FDG PET outcome measures (i.e., SUVR vs. CMRGlu), the spatial pattern of glucose metabolism within a subject is the same because SUVR and CMRGlu are based on the same underlying [^{18}F]FDG uptake. There is only a difference in the amplitude by scaling between the whole brain uptake for SUVR and the arterial input function (AIF) for CMRGlu (Godbersen et al., 2024). This equality of the spatial pattern of different metabolic metrics within a subject implies that the

spatial correlation with FC also yields identical results. Initially, a target region was selected from an atlas with k regions. FC was then computed between BOLD signal time courses of the target region and all of the remaining k-1 brain regions, followed by z-transformation. This was done for each voxel of the target region, yielding k-1 voxel-wise FC patterns of the target region. To account for the high degree of correlation between the input signals of the different brain regions, principal component analysis (PCA) was applied to the FC patterns. This results in k-1 orthogonal principal components that represent linear combinations of FC patterns (PC_{FC}). Next, the spatial correlation between the k-1 orthogonal voxel-wise PC_{FC} patterns and the voxel-wise CMRGlu pattern in the target region was calculated. This yields k-1 MCM r-values, which were then transformed to the coefficient of determination r^2 as a metric of explained variance. Since a simple summation of all k-1 r^2 values would reach nearly 100% explained CMRGlu for a sufficient number of input signals, we employed two different approaches to sum only relevant or non-randomly occurring variance, respectively. First, the elbow criterion was used, which discards signals that do not add relevant explained variance (Approach a in Fig. 1). Basically, in a plot of decreasingly explained variance, the point with the minimum distance to the origin is selected. This is computationally fast and was used as a basis for subsequent calculations. A second, more sophisticated approach was employed for validation to ensure that the explained CMRGlu is not influenced by the estimation of the elbow point (Approach b in Fig. 1). Here, the k-1 voxel-wise FC patterns in the target were randomly permuted, subject to PCA and correlated with the voxel-wise CMRGlu pattern of the target region. Permutations were repeated $j = 500$ times, which resulted in (k-1)*j random MCM correlation values. For each permutation, only the maximum value across all k-1 MCM values was selected to create a random distribution. Assigning the top 5% of permuted MCM values as a cutoff has strong control for type-I statistical errors at $p < 0.05$ FWE-corrected (Genovese et al., 2002; Holmes et al., 1996). Thus, to obtain the total amount of explained CMRGlu, only r^2 values above the mentioned thresholds were summed and then assigned to the one target region. Finally, repeating the entire algorithm k times and each time assigning a different brain region as a target gives a whole-brain estimate of explained CMRGlu by FC input signals.

On the other hand, we assessed the contribution of an input region's FC to explain CMRGlu (Suppl. Fig. 1b). Here, for each PC_{FC} with an r^2 value higher than random, this r^2 value was first evenly divided by k-1 input regions, then weighted by the normalized PCA coefficients and finally assigned back to the brain regions. This is feasible since the PCA coefficients represent the individual contribution of each input variable (in this case FC) to the PC. The explanatory capacity of a region's FC was then subtracted from its explained CMRGlu to determine if a region is preferentially "incoming" (explained CMRGlu > explaining FC), "outgoing" (explained CMRGlu < explaining FC) or "indifferent" (explained CMRGlu = explaining FC).

We want to highlight that the target region's FC was obviously excluded from the above calculations, thus avoiding a simple autocorrelation effect.

2.10. Network optimization

For MCM and FC data, directed and undirected connectivity matrices of 200×200 regions were computed, respectively. These were averaged across subjects and separately subject to optimization with the Louvain algorithm as implemented in the brain connectivity toolbox (https://sites.google.com/site/bctnet/home). The algorithm maximizes edges within a module and minimizes edges between modules, resulting in an optimal community structure. As the Louvain algorithm is not deterministic, the structure with the maximum community statistic Q out of 1000 runs was chosen with subsequent iterative fine-tuning as suggested in the brain connectivity toolbox. The two network partitions obtained with MCM and FC data were then compared with respect to their within-module weighted efficiencies (Hearne et al., 2017). For the MCM network partitions, the explained CMRGlu and within-module efficiency were subsequently computed for each condition (rest vs. task) and cohort (young vs. elderly).

2.11. Gene expression

Processing of mRNA gene expression data was carried out as described previously (Komorowski et al., 2022). In short, mRNA data from the Allen Human Brain Atlas (http://human.brain-map.org/) (Hawrylycz et al., 2012; Shen et al., 2012a) were interpolated, yielding high-resolution whole-brain maps of gene expression (log2), which are publicly available (http://www.meduniwien.ac.at/neuroimaging/mRNA.html) (Gryglewski et al., 2018). These maps were matched with Entrez Gene IDs, and in this study, only neuro-related genes were used (Diez and Sepulcre, 2018), resulting in 3206 genes. From these maps, average regional values were extracted with the Craddock-200 atlas.

2.12. Synaptic vesicle protein 2A (SV2A) PET

A group-average voxel-wise map of [^{11}C]UCB-J total volume of distribution (VT) was kindly provided by Richard E. Carson, Yale PET Center, New Haven, USA. The map was created as an average of $n = 30$ healthy volunteers (aged 26.2 ± 3.6 years, 14 females), and the radioligand is specific for SV2A (Rossano et al., 2020; Yu, 2022). Average regional values for the Craddock-200 atlas were extracted and used for statistical analysis.

2.13. Aerobic glycolysis

Group-average data of the oxygen-to-glucose index (OGI) was kindly provided by Manu Goyal and Andrei Vlassenko, Washington University School of Medicine, St. Louis, USA. Data were collected from $n = 30$ healthy volunteers (aged 25–45 years, 14 females). Briefly, PET data were acquired after administration of [^{18}F]FDG as well as [^{15}O]O_2, [^{15}O]H_2O and [^{15}O]CO. Glucose and oxygen metabolism ($CMRO_2$) were estimated as SUVR with reference to the whole brain using the Schaefer 200 atlas for cortical regions and FreeSurfer for subcortical and cerebellar regions, respectively. Correction for partial volume effects was carried out with the symmetric GTM algorithm. Relative OGI was then calculated by dividing $CMRO_2$ by glucose metabolism. For further details, please see (Goyal et al., 2023). Since OGI data was averaged across young healthy adults without atrophy, correction for partial volume effects will only scale (i.e., consistently increase) the values. This is, however, unlikely to affect the association with explained CMRGlu, since a correlation is independent of the amplitude.

2.14. Statistical analysis

In general, statistics were calculated in Matlab using the Craddock atlas with $k = 200$ brain regions and by deriving explained CMRGlu with the elbow criterion unless specified otherwise. Differences in explained CMRGlu from the whole-brain average, between conditions (rest vs. task), and between groups (young vs. elderly) were computed with random permutations (Fig. 2). Here, $m = 5000$ permutations were used. For $k = 200$ regions, only the maximum and minimum values were saved for each permutation. Random distributions were built with these two extreme values, and significance was declared if observed values exceeded the top 2.5% of random values, yielding two-tailed control for type-I statistical errors with FWE correction (Genovese et al., 2002; Holmes et al., 1996). Similarly, this approach was used for the evaluation of differences in the FC's contribution to explain CMRGlu (Fig. 4) and for assigning directionality to brain regions (Fig. 5). To assess differences in the distribution of explained CMRGlu between young and elderly cohorts, an F-test for equal variances was computed.

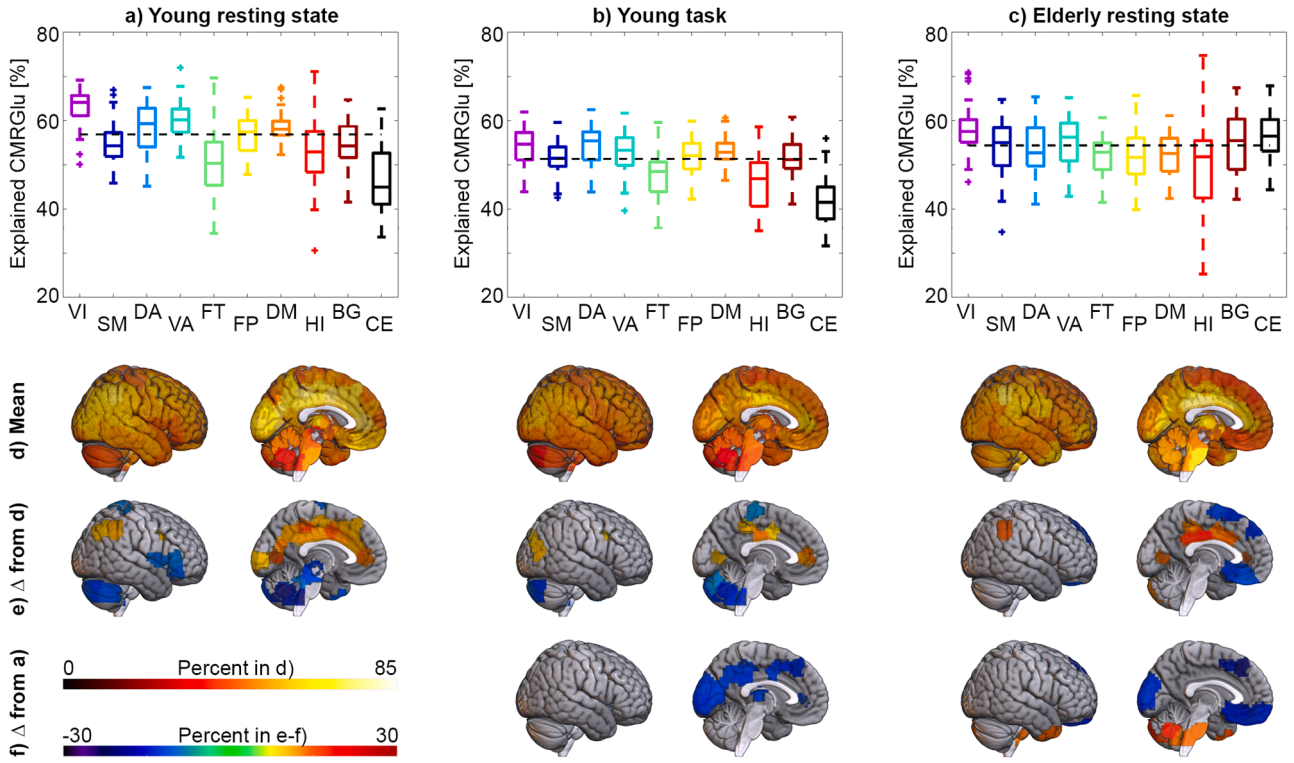

Fig. 2. *Explained glucose metabolism (CMRGlu) by functional connectivity (FC).* Young adults at resting state showed considerable regional variation between 34.0 and 76.1% (a and d). Higher than average values were observed, particularly in the visual, cingulate, and frontal cortices, with lower values in the cerebellum and subcortical areas (e). During the performance of the visuospatial cognitive task Tetris® (b, d, e), regionally-specific decreases were found particularly in the occipital cortex, fusiform gyrus, and posterior cingulate (f). In healthy elderly subjects, there was a marked decrease in regional variation (c, d, e), mostly driven by increases in subcortical areas and the cerebellum (f). Differences in e and f are corrected for multiple comparisons at $p < 0.05$ FWE using random permutations. Results were obtained with the Craddock 200 atlas. Network parcellation, VI: Visual, SM: somatomotor, DA: dorsal attention, VA: ventral attention, FT: frontotemporal, FP: frontoparietal, DM: default mode (as provided in (Yeo et al., 2011)), HI: hippocampus/amygdala, BG: basal ganglia/striatum, CE: cerebellum (Harvard Oxford Atlas as provided in FSL).

To evaluate associations between explained CMRGlu and mRNA expressions (Fig. 3), Spearman's correlations were computed across brain regions, which were then subject to a gene-category enrichment analysis (Komorowski et al., 2022). This was realized with the GO knowledgebase (Ashburner and Lewis, 2002; The Gene Ontology Consortium, 2019) using categories of biological processes. Gene expression patterns were assigned a gene score based on correlation values, and ensemble-based null models were calculated (Fulcher et al., 2021). Thus, GO categories representing a significant association with explained CMRGlu were identified using gene category enrichment analysis with a random permutation approach and adjustment for multiple testing with the Benjamini-Hochberg procedure. Associations of explained CMRGlu with [^{11}C]UCB-J SV2A and OGI were computed with Pearson's correlation across brain regions (Fig. 3). For the above associations with mRNA expressions, SV2A and OGI data and regional values were weighted by region size. This was used to avoid bias of

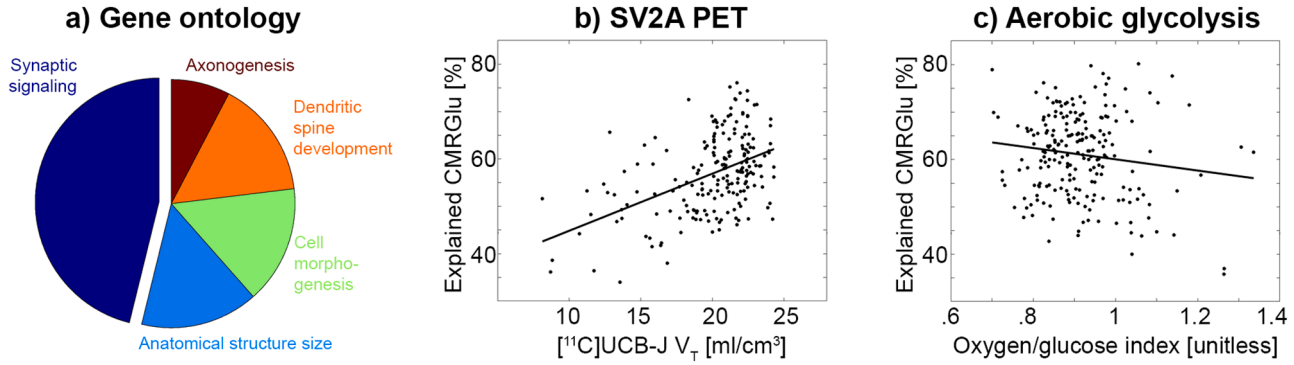

Fig. 3. *Association of explained CMRGlu with synaptic signaling.* The spatial distribution of explained CMRGlu in young adults at rest (Fig. 2a and d) was correlated to the mRNA gene expression and significant associations were further used for gene category enrichment analysis, which yielded Gene Ontology (GO) terms mainly depicting synaptic and anatomical respective morphological functions (a, all corrected for multiple comparisons using random permutations). 'Synaptic signaling', 'anatomical structure size', 'cell morphogenesis', 'dendritic spine development' and 'axogenesis' are the short forms or overlapping themes of the respective GO categories (see Suppl. Tab. S2 for details). The explained CMRGlu was positively associated with synaptic density indexed by [^{11}C]UCB-J PET synaptic vesicular glycoprotein 2A (SV2A) binding (Rossano et al., 2020) (b, $r = 0.49$, $p < 10^{-4}$) and negatively associated with oxygen-to-glucose index (c, $r = -0.52$, $p < 10^{-4}$) across brain regions. mRNA and SV2A results were obtained with the Craddock 200 atlas. OGI data were obtained with the Schaefer 200 atlas.

different region volumes and to enable comparison between different atlases, as the OGI data was only available for the Schaefer 200 atlas with FreeSurfer subcortical/cerebellar parcellation.

Comparison of within-module weighted efficiencies between MCM and FC network partitions was carried out by paired *t*-tests (Suppl. Fig. S3). This was repeated after deleting regions of the MCM-based module 4 (see results). For the MCM-based network partitions, a comparison of explained CMRGlu and efficiency was done with repeated measures ANOVA with the module as a factor and subsequently paired *t*-tests (Fig. 6).

Differences between the two approaches to determine explained CMRGlu (elbow criterion vs. random permutations) were assessed by Pearson correlation across brain regions (Suppl. Fig. S2). In a similar manner, parcellation schemes were compared, where smaller regions were downsampled to larger ones by calculating a weighted average of explained CMRGlu.

3. Results

All results were obtained with the Craddock 200 atlas, unless specified otherwise (see Suppl. Fig. S2 for further parcellations).

3.1. Regionally specific associations between CMRGlu and PC_{FC}

First, we determined the overall ability of FC to explain CMRGlu as schematically shown in Fig. 1. For an atlas with k regions and any given target region, FC with all other brain regions was calculated, yielding (k-1) voxel-wise FC patterns in the target region. To account for the high degree of correlation between the different input signals, principal component analysis (PCA) was applied to these FC patterns. This results in k-1 PCs, which represent linear combinations of FC patterns (PC_{FC}). MCM was then calculated as (k-1) spatial correlations between the voxel-wise CMRGlu pattern and all PC_{FC} patterns, which were converted to the coefficient of determination (r^2) as a metric of explained variance. Only those values exhibiting relevant r^2 (estimated by elbow criterion or random permutations) were summed and assigned to the target region.

At rest, the explained variance of CMRGlu by FC was highly heterogeneous across brain regions (Fig. 2a, d and e). The highest values were observed in cortical regions with peak values of up to 76.1 ± 13.3% (mean±sd across subjects) in the visual network and the lowest in subcortical areas and the cerebellum (34.0 ± 16.5%). Compared to the global mean of 56.9% at resting state, significant increases were observed in the visual, cingulate, and frontal cortices. In contrast, decreases occurred in the subcortical areas and cerebellum (Fig. 2e). This regional variation is non-trivial from a computational point of view since for any two brain regions, k-2 input signals (e.g., 99% of input signals for an atlas with $k = 200$ regions) are identical. The pattern of explained variance was robust against different parcellation schemes, the number of brain regions, and the approach to account for randomly explained variance (Suppl. Fig. S2).

We then investigated alterations in the explained CMRGlu induced by cognitive performance and in healthy aging (all $p < 0.05$ FWE corrected). During task execution, specific decreases as low as −17% were found in the occipital cortex, fusiform gyrus, anterior and posterior cingulate cortices (Fig 2b, d, e and f). In contrast, healthy elderly subjects showed a de-differentiation in the explained CMRGlu across brain networks (variance test $p < 0.05$, Fig. 2c and d). This was driven by increases in the cerebellum and subcortical regions of up to 26% but decreases of 23% in medial and dorsolateral prefrontal areas compared to young adults (Fig. 2f).

To rule out that effects in the elderly cohort were driven by amyloid accumulation, [^{18}F]AV-45 amyloid scans were obtained from the ADNI database. Average SUVR was 1.03 ± 0.20, with 11 subjects being amyloid positive, regardless of the threshold (Farrell et al., 2021; Mormino, 2014). There was no significant difference in explained CMRGlu between amyloid positive and negative subjects ($p = 0.47$).

3.2. Explained CMRGlu relates to synaptic processing and aerobic glycolysis

Next, we aimed to identify the neurophysiological underpinnings of the association between FC and CMRGlu. The regional distribution of explained CMRGlu (Fig 2a and d) was related to that of mRNA expressions of 3206 neuro-related genes (Diez and Sepulcre, 2018). This revealed associations particularly with genes involved in synaptic signaling and transmission-associated processes (Fig. 3a, Table S2, all $p < 0.05$ corrected). In line, the explained CMRGlu was also correlated with synaptic vesicle glycoprotein 2A binding as derived from [^{11}C] UCB-J PET imaging (Rossano et al., 2020) ($r = 0.49$, $p < 10^{-4}$, Fig. 3b). Finally, we observed a negative association with the OGI (Goyal et al., 2023) (low OGI reflects high AG, $r = -0.52$, $p < 10^{-4}$, Schaefer 200 atlas). Together, these findings indicate that the ability of FC to explain CMRGlu is linked to the underlying synaptic connections and signaling processes, which is in line with the main assumption of MCM that metabolic demands are predominantly driven by postsynaptic signaling. Further, these signaling processes seem to be at least partly fueled by aerobic glycolysis.

3.3. Distinct contributions of functional connectivity

We also evaluated the explanatory capacity of each brain region's FC by assigning r^2-values to input regions (instead of computing the maximum amount of explained CMRGlu by summing up r^2 in target regions as above). This was realized by distributing the non-random r^2-values across all input brain regions after weighting them according to their individual contributions, as given by the PCA coefficients. The approach enabled us to investigate the contributions of FC to explain CMRGlu between networks (Fig. 4). Overall, the analysis revealed higher within- than between-network contributions, independent of the condition (rest and task, main effect $p < 10^{-4}$) and cohort (young and elderly, $p < 10^{-4}$), showing that FC within a network explains more CMRGlu than FC of other networks (Fig. 4a, d-e). Compared to resting state, task execution exclusively elicited decreases in the FC's contribution (Fig. 4b). This was more pronounced for within- than between-network associations (interaction $p < 10^{-4}$, Fig. 4d), indicating a decreased segregation of networks during cognitive performance. The observation is also supported by the correlation of within vs. between network associations with task scoring, where subjects with less segregation performed better ($r = -0.46$, $p < 0.001$, Fig. 4f). In contrast, elderly subjects showed increased associations, particularly for those networks with low values of explained CMRGlu and decreased associations within networks (Fig. 4c and e).

In a second step, we calculated the relationship between how much CMRGlu is explained in a region vs. how much a region explains by its FC. We designated regions as "incoming" if its explained CMRGlu is higher than its explained FC, as "outgoing" if vice versa, and as "indifferent" if the difference was not significant ($p < 0.05$ FWE corrected). At resting-state hippocampal and basal ganglia networks were preferentially incoming (Fig. 5a), which was, however, inverted during task performance (Fig. 5b). In line with the low amount of explained CMRGlu, the cerebellum comprised mostly outgoing regions for both conditions. In elderly subjects, the majority of brain regions showed indifferent behavior, except for the hippocampal network being preferentially outgoing (Fig. 5c). The ventral attention network was stable incoming across conditions and cohorts.

3.4. CMRGlu refines brain network organization

Finally, we assessed whether the incorporation of CMRGlu allows a refined definition of functional brain networks. Average whole-brain connectivity matrices of resting-state FC and explained CMRGlu using MCM were separately optimized by maximizing within module edges and minimizing between module edges (Louvain algorithm). This

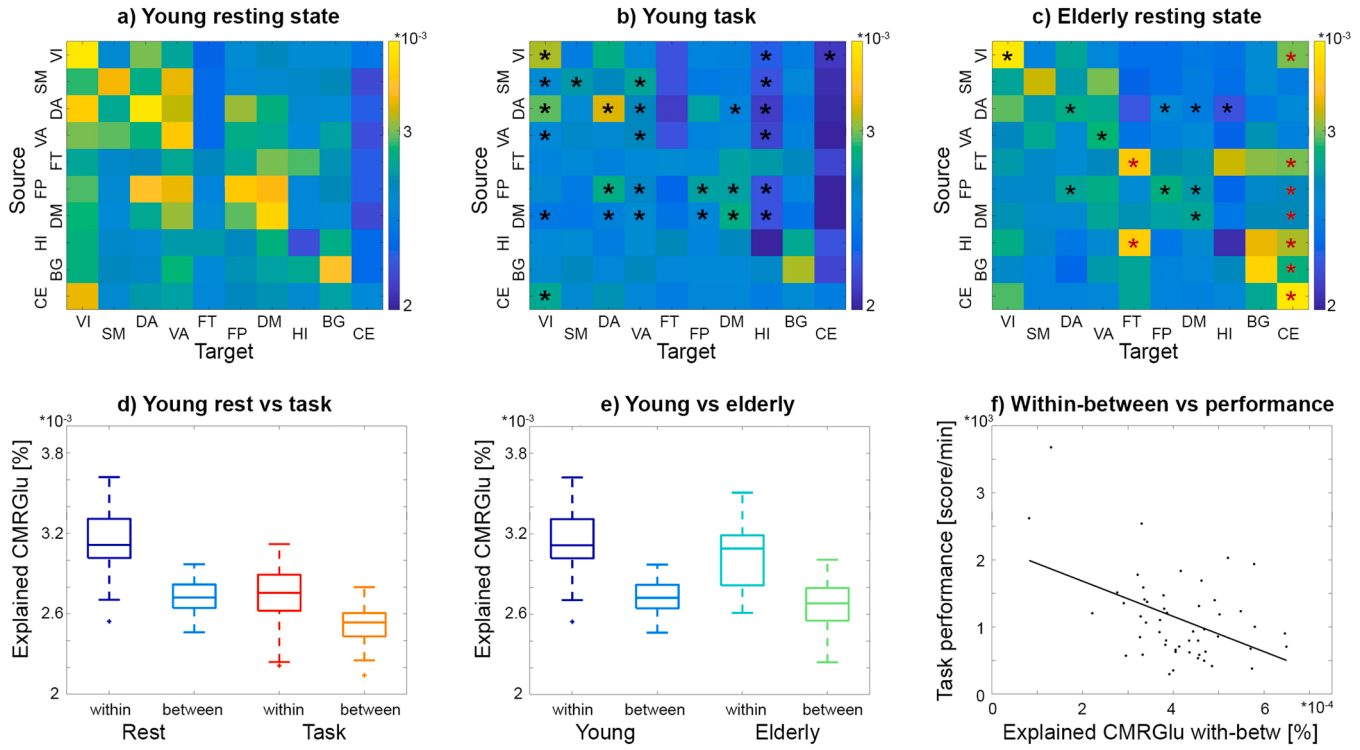

Fig. 4. *Within- and between network differences in explained CMRGlu.* Matrices show pairwise contributions of FC (source, rows) to explain CMRGlu (target, columns) between networks (a-c). Overall, FC within a network explained more CMRGlu than FC between networks independent of condition (rest and task, d: main effect $p < 10^{-4}$) and cohort (young and elderly, e: $p < 10^{-4}$). Task performance resulted in decreased values of explained CMRGlu, particularly for within-network effects (b, d: interaction $p < 10^{-4}$). The difference within-between network contributions also correlated with task performance (f: $r = -0.47$, $p < 0.001$). Elderly subjects showed increased associations, particularly for networks with low values of explained CMRGlu and increases within networks (c). Asterisks in b and c indicate significant decreases (black) or increases (red) compared to a. Results were obtained with the Craddock 200 atlas. Network parcellation, VI: Visual, SM: somatomotor, DA: dorsal attention, VA: ventral attention, FT: frontotemporal, FP: frontoparietal, DM: default mode (as provided in (Yeo et al., 2011)), HI: hippocampus/amygdala, BG: basal ganglia/striatum, CE: cerebellum (Harvard Oxford Atlas as provided in FSL).

resulted in two network definitions comprising 4 and 3 modules for MCM- and FC-based partitions, respectively (Fig. 6a, Suppl. Fig. S3a-b). As expected, for individual MCM data, the corresponding MCM-based module definition exhibited higher within-module efficiency than FC-based partitioning (Suppl. Fig. S3c, $p < 10^{-4}$). Crucially, even for FC data, the MCM-based module definition yielded higher efficiency (Suppl. Fig. S3d, $p < 10^{-4}$). Aiming to identify this difference's source, we simulated the elimination of all regions of module 4 as obtained from the MCM-based definition (see rationale below). This increased the efficiency of FC-based partitioning to the same level as MCM-based definition for both MCM and FC data (Suppl. Fig. S3c-d, both $p > 0.3$). Thus, differences in efficiency were indeed driven by module 4, which was, however, only achieved through consideration of CMRGlu in the computations.

Topologically characterizing the MCM-based partitions (Fig. 6a) showed that module 1 comprised visual and posterior dorsal attention networks, whereas module 2 included somatomotor as well as ventral and dorsal attention networks. Module 3 mostly comprised the frontoparietal and default mode networks, which are considered to be antagonistic (Buckner and DiNicola, 2019; Murphy and Fox, 2017). Module 4 largely summarized brain networks with the lowest values of explained CMRGlu, i.e., subcortical regions, the cerebellum, and the frontotemporal network (Fig. 6b, rmANOVA $p < 10^{-4}$). This separation of module 4 was also observed during task performance (Fig. 6c, rmANOVA $p < 10^{-4}$). However, in healthy elderly subjects, module 3, comprising default mode and frontoparietal networks, showed the lowest explained CMRGlu (Fig. 6d, rmANOVA $p < 10^{-4}$). A similar effect was obtained when investigating the within-module efficiency, with module 3 in healthy elderly exhibiting the lowest values (Fig. 6g, rmANOVA $p < 10^{-4}$), which was, however, not the case for young adults at rest (Fig. 6e) or during task execution (Fig. 6f).

4. Discussion

Based on the physiological relationships between signaling and energy demands, we modeled whole-brain functional connectivity as input signals to explain postsynaptic glucose metabolism. This provides a global perspective on how remote brain networks shape local energy demands.

4.1. *CMRGlu-PC_{FC} relation reflects non-oxidative metabolic demands of signaling input*

Our approach revealed substantial regional variation in this association ranging from 34% in the cerebellum to 76% in the visual cortex. Interestingly, these regional differences were associated with the patterns of non-oxidative energy metabolism, i.e., the oxygen-to-glucose index (OGI), depicting aerobic glycolysis (AG). AG represents almost 25% of glucose consumption in the resting human prefrontal cortex and only 2% in the cerebellum (Vaishnavi et al., 2010). Although AG is an ATP-inefficient way of energy supply, it has been shown to occur abundantly in glutamatergic and GABA-ergic neurons, astrocytes (Dienel, 2019) as well as during synaptic transmission (Yu et al., 2018), synaptic remodeling and learning (Shannon et al., 2016).

Most recently, a tight coupling of the BOLD signal with AG has been proposed (Theriault et al., 2021) (but see other examples that showed dissociations between the BOLD signal and metabolism (DiNuzzo et al., 2022; Koush et al., 2021; Stiernman et al., 2021)). Thereby, BOLD

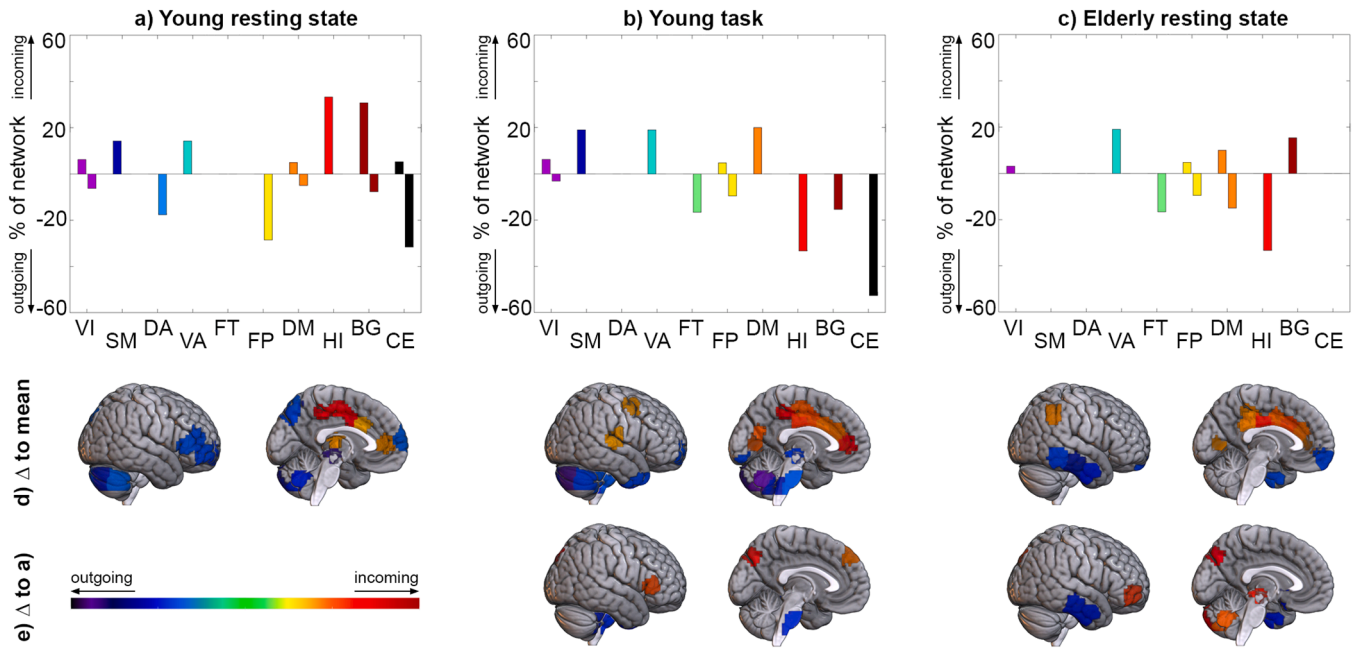

Fig. 5. *Relationship between a brain network's explained CMRGlu by remote FC vs. the ability of the network's FC to explain remote CMRGlu.* a-c) Regions of a network were designated as "incoming" if the normalized explained CMRGlu is higher than the normalized explaining FC (positive values) or as "outgoing" if vice versa (negative values), expressed as a percentage of the spatial extent of a given network. The remaining amount to match 100% were regions without significant differences between the two parameters ("indifferent"). Colors match those of boxplots in Figure 2; see Figure 2 for abbreviations. d) Visualization of the brain regions with significantly higher than average explained CMRGlu (incoming) or higher than average explaining FC (outgoing). f) Visualization of the brain regions with significant differences to young adults at resting state. All values are corrected at $p < 0.05$ FWE using random permutations; differences in d and e are given in arbitrary units. Results were obtained with the Craddock 200 atlas. Network parcellation, VI: Visual, SM: somatomotor, DA: dorsal attention, VA: ventral attention, FT: fronto-temporal, FP: frontoparietal, DM: default mode (as provided in (Yeo et al., 2011)), HI: hippocampus/amygdala, BG: basal ganglia/striatum, CE: cerebellum (Harvard Oxford Atlas as provided in FSL).

signals reflect interregional error signaling, supported by fast-spiking parvalbumin-positive interneurons (FSP+) (Buzsáki and Wang, 2012), which mainly rely on non-oxidative metabolism since their thin axons do not provide sufficient space for mitochondria (Theriault et al., 2021). From this perspective, the BOLD signal reflects rapid non-oxidative metabolic fluctuations of FSP+-synchronized neuronal signaling (Theriault et al., 2021). Given the closely matching patterns of PC_{FC} explaining CMRGlu and AG, we follow Theriault et al. in the assumption that FC represents mainly interregional on-demand processing fueled by AG. This is also in line with the BOLD signal being responsible for about 5% of the changes in net ATP production (Raichle, 2010). As our model builds on overall linear combinations of FC input and correlates with the regional pattern of AG, it seems to explain a minor yet critical proportion of overall metabolic turnover (Vaishnavi et al., 2010), whereas the metabolic baseload is covered by energy-efficient but slow oxidative phosphorylation (Theriault et al., 2021).

In addition, different ratios of excitatory (AMPA, M1) to inhibitory (GABA-A, M2) receptor density across the brain relate to functional connectivity (Rajkumar et al., 2021; van den Heuvel et al., 2016). In the cerebellum, about 70% of energy metabolism relates to excitatory neurons (Howarth et al., 2012, 2010), whereas GABA-A density (Nørgaard et al., 2021) and inhibitory neurons are low (Howarth et al., 2012). Again, the cerebellum showed the least explained CMRGlu and low AG (Vaishnavi et al., 2010). Hence, we speculate that regional differences in postsynaptic energy demand explained by PC_{FC} emerge from a different proportion of AG in overall metabolism due to different densities of FSP+ interneurons which, in turn, receive excitatory FC input by remote functional projections. This excitatory input to FSP+ is in line with the intimate relationship between postsynaptic AMPA receptors and energy demands (Harris et al., 2012) and the expression of these receptors on FSP+ (Homayoun and Moghaddam, 2007; Kooijmans et al., 2014). The interpretation that FC input relates to synaptic signaling is also supported by imaging transcriptomics (Diez and Sepulcre, 2018; Martins et al., 2021), where genes primarily involved in synaptic signaling were related to the explained CMRGlu (Chen et al., 2021; Goyal et al., 2014). Furthermore, an association was observed with the regional distribution of SV2A, a marker for synaptic density (Carson et al., 2022; Finnema et al., 2016), which also correlates with regional variation of [^{18}F]FDG metabolism (Chen et al., 2021; Yu, 2022), AG (van Aalst et al., 2021) and excitatory synaptic signaling obtained from 1H-MRS glutamate imaging (Onwordi et al., 2021). Together, these findings suggest that CMRGlu explained via PC_{FC} input reflects the metabolic cost of incoming excitatory synaptic signals, i.e., functional input via glutamatergic neurons. The close link between glutamate release, neurovascular coupling (Attwell et al., 2010; Mishra et al., 2016) and neuronal (Lundgaard et al., 2015) as well as astrocytic (Zimmer et al., 2017) glucose uptake (Harris et al., 2012; Magistretti and Allaman, 2015; Raichle and Mintun, 2006), further supports this interpretation (Klug et al., 2022).

4.2. *Signaling input shapes explained metabolism during task performance and in healthy aging*

Independent of task condition and age, the metabolic cost of a network was mainly defined by its own FC instead of functional inputs from other networks. This corresponds to the segregated brain organization at rest, representing a metabolically optimized state (Raichle, 2015) to enable flexible network reconfiguration when engaged in cognitive tasks (Hearne et al., 2017; Wig, 2017). In line, we observed a shift to a more integrated network structure (i.e., desegregation) during cognitive task performance (Cohen et al., 2014; Cohen and D'Esposito, 2016; Cole et al., 2014; Krienen et al., 2014; Mattar et al., 2015; Shine et al., 2016; Spadone et al., 2015; Westphal et al., 2017), specifically in regions involved in the execution of the Tetris® task (Agren et al., 2021;

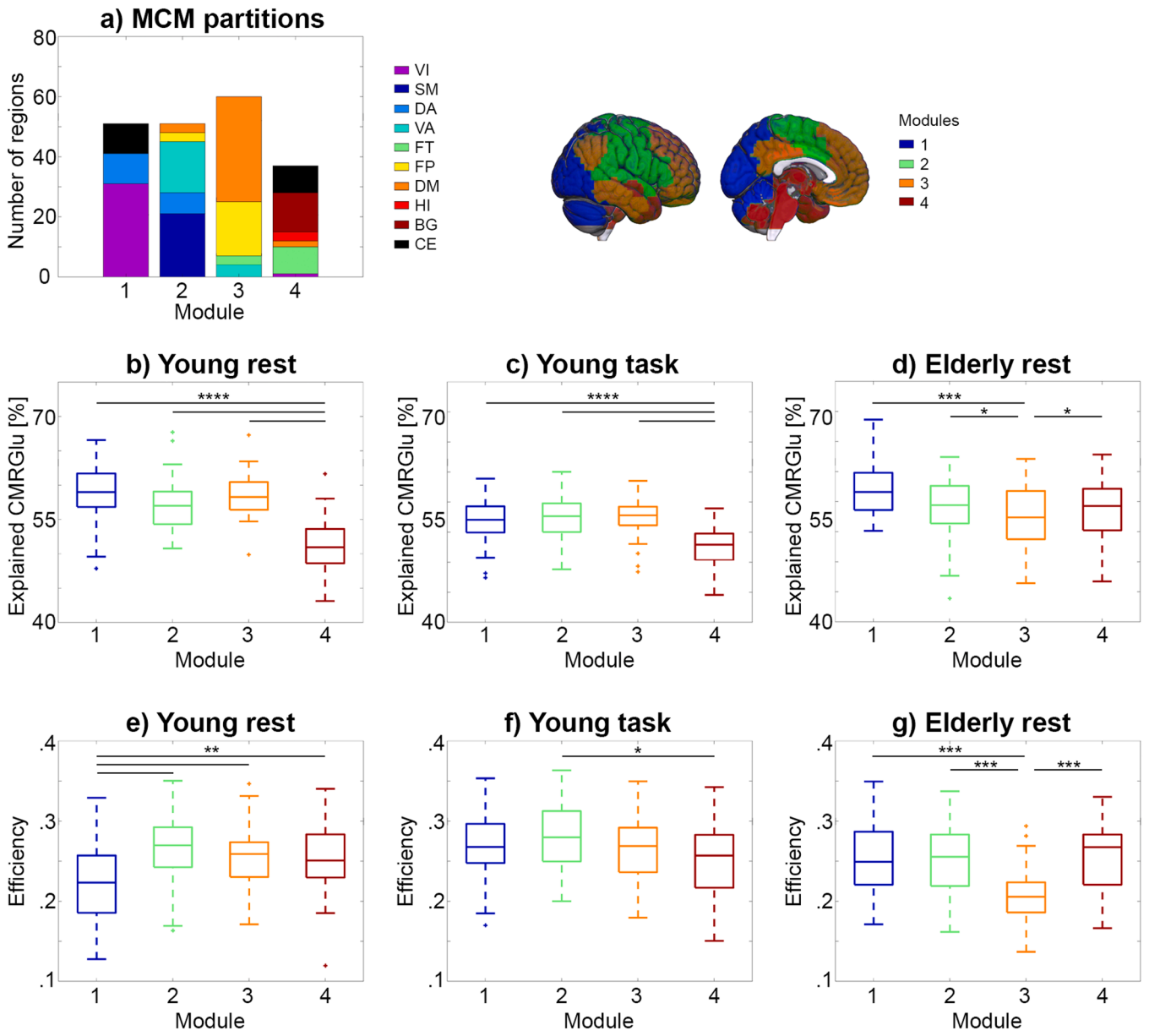

Fig. 6. *CMRGlu enables refined network partitioning.* Optimization of average MCM-based whole-brain connectivity matrices resulted in a 4-module solution (a). For young participants at rest (b) and during task performance (c), module 4 summarized networks with the lowest explained CMRGlu (rmANOVA both $p < 10^{-4}$). However, in elderly individuals, module 3 showed the lowest values for explained CMRGlu (d, rmANOVA $p < 10^{-4}$) and efficiency (g, rmANOVA $p < 10^{-4}$). Colors and abbreviations match those of boxplots in Figure 2. Results were obtained with the Craddock 200 atlas. VI: Visual, SM: somatomotor, DA: dorsal attention, VA: ventral attention, FT: frontotemporal, FP: frontoparietal, DM: default mode (as provided in (Yeo et al., 2011)), HI: hippocampus/amygdala, BG: basal ganglia/striatum, CE: cerebellum (Harvard Oxford Atlas as provided in FSL).

Hahn et al., 2020) such as visual processing and attention (Sheth and Young, 2016). This emerged from a stronger decrease of input from within than between-network connections. Better task performance was also correlated with relatively higher integration of networks in this and previous studies (Cohen and D'Esposito, 2016; Gratton et al., 2016; Schultz and Cole, 2016; Shine et al., 2016; Westphal et al., 2017). Following the above interpretations on a neuronal level, FSP+ interneurons have been shown to increase their firing rate during action execution (Gage et al., 2010) and to enable between-network interactions through initiating coordinated oscillations across networks (Roux and Buzsáki, 2015), which crucially contributes to task performance during early learning (Lee et al., 2017). Hence, we speculate that FSP+ interneurons enable the fast reorganization of between-network interactions during task performance, leading to increased integration. We suppose that this modulation of network interaction reflects cognitive flexibility, as signified by rapid on/off peaks of brain activity (and metabolism via AG) (Theriault et al., 2021), representing an essential capacity for the execution of cognitive tasks.

In contrast to young adults, elderly individuals showed a high similarity of explained CMRGlu across brain networks, i.e., dedifferentiation. Healthy human aging has been associated with region-specific changes in glucose metabolism (Deery et al., 2023a; Shen et al., 2012b) and desegregation of brain networks (Deery et al., 2023b; Geerligs et al., 2015). Dedifferentiation with aging was also observed for metabolically-defined networks (termed "metabolic homogeneity") (Arnemann et al., 2017) and BOLD variability, which has been linked to cognitive decline (Garrett et al., 2011) and associated with deficits in dynamically exploring functional brain states (Deco et al., 2011). Accordingly, the decreased segregation in elderly subjects might indicate an impaired network reconfiguration and reduced cognitive

flexibility (Goyal et al., 2017). Even though regions with pronounced AG have been shown to exhibit increased amyloid deposition (Vlassenko et al., 2010), our analysis did not indicate differences in explained CMRGlu between amyloid positive and negative elderly subjects. Given the above association of explained CMRGlu with AG and a flattened AG pattern in the elderly (Goyal et al., 2017), we interpret this result as dedifferentiation of non-oxidative metabolism, possibly explaining reduced cognitive flexibility. Considering the independence of this flattened AG pattern from the amyloid status of elderly subjects marks it as a more general feature of aging. As indicated above, a high amount of explained CMRGlu potentially reflects high synaptic signaling input to FSP+ fueled by AG. Thus, vulnerable cortical regions with distinctly decreased AG (Goyal et al., 2014) may experience pronounced loss of FSP+ (Theriault et al., 2021), resulting in reduced inhibition of excitatory pyramidal neurons. This is in line with recent propositions for hypersynchrony in brain networks of AD patients due to FSP+ dysfunction (Palop and Mucke, 2016). Furthermore, AG-vulnerable areas exhibit higher-order cognitive control (Blazey et al., 2019), which may subsequently elicit increased firing via (disinhibited) excitatory projections to subcortical and cerebellar regions with relatively stable amounts of AG. This increased higher-order signaling aligns with the hypothesis for a shift in functional connectivity to compensate for reduced flexibility in the aging brain (Davis et al., 2008; Deery et al., 2023b; Spreng and Turner, 2019).

4.3. Characterizing brain networks by their dynamic energy demands

In the following, we apply our interpretation of whole-brain FC input as the primary driver of non-oxidative postsynaptic metabolism to characterize the interrelation of brain networks. Thereby, we extend prevailing approaches, which rely on FC (Yeo et al., 2011) or CMRGlu alone (Arnemann et al., 2017).

Incorporating metabolic information into connectivity provides complementary information to previous work (Avena-Koenigsberger et al., 2019; Ito et al., 2017), where functional and structural metrics defined networks as preferentially sending or receiving information (Seguin et al., 2019). Interestingly, the direction of our metabolically defined directionality runs opposite to the previous one (Seguin et al., 2019) and a connectivity gradient from primary sensory and motor regions to the default mode network (Margulies et al., 2016). Following a predictive processing interpretation of this gradient (Katsumi et al., 2022), it seems that metabolically defined “incoming” and “outgoing” signals essentially characterize top-down predictions, which run opposite to the main direction of connectivity (Seguin et al., 2019) and may reflect a crucial proportion of directed connections that enable network interactions. This is based on the abovementioned interpretations, where BOLD FC input fueled by AG through FSP+ may essentially represent predictive processing (Theriault et al., 2021). Indeed, FSP+ are considerably involved in prediction error circuits (Hertäg and Clopath, 2022; Hertäg and Sprekeler, 2020; Yau et al., 2021). Thereby, excitatory signals from higher-order brain regions to FSP+ of lower-order regions have been interpreted as signals that update prediction errors (Barron et al., 2020).

Interestingly, these directed prediction signals changed during task execution. For instance, the output of FP and DA substantially decreased, which might be explained by an increased error signaling during the task, leading to a perturbation of outgoing predictions. The reduced prediction output of DA is in line with former results showing increased feedforward processing (i.e., prediction error signaling) from the occipital cortex to DA (Hahn et al., 2020).

In accordance with altered predictive processing in the aging brain (Chan et al., 2021; Hsu et al., 2021), elderly subjects showed an overall flattening of interregional predictions. These were primarily driven by decreased outputs of CER, FP, and DA, as well as decreased inputs to BG and SM. In line, aging was associated with reduced interactions between the cerebellum, basal ganglia, and cortical regions (Brown et al., 2022). This has been linked (Brown et al., 2022) to the default–executive coupling hypothesis of aging (Turner and Spreng, 2015), which might explain the observed shift to DM output in elderly HC. Thereby, reductions of CER-BG-cortical interactions have been associated with reduced updating of cortical routines (Brown et al., 2022), while increased executive-DM synchrony was linked to increased retrieval of already proven predictions in elderly (Brown et al., 2022).

Finally, investigating the impact of metabolic demands on the formation of brain networks, we identified that regions with the lowest explained CMRGlu proved responsible for suboptimal efficiency in FC-based network definitions. As efficiency again increased upon the elimination of these regions, our findings indicate that brain metabolism carries unique information for optimized large-scale network partitioning. Given the association of FC explaining CMRGlu with synaptic density and signaling processes, we assume that this network optimization was primarily driven by the corresponding synaptic signaling input. Previous network refinement has demonstrated that regions may indeed contribute to multiple networks (Bijsterbosch et al., 2019; Yeo et al., 2016). Interestingly, the topography of our MCM-based module partitions closely resembles a former optimization of network organization (Cookson and D’Esposito, 2022). This included an overlap of DM and FP, which are usually thought to operate antagonistically (Buckner and DiNicola, 2019; Murphy and Fox, 2017), as well as the fusion of SM, VA, and anterior DA. In addition, the observed DMN split is in line with formerly identified subsystems of core, medial temporal and dorsal medial subsystems (Smallwood et al., 2021). Moreover, the combination of VI and posterior DA aligns with previous work, which showed better task performance for subjects with increased resting state functional connectivity between task-positive regions (Baldassarre et al., 2012).

Interestingly, these new partitions also showed age-related changes. Within-module efficiency increased for module 1 (i.e., VI and DA) but decreased for module 3 (DM and FP). This is in line with observations of decreased DM and FP connectivity as well as increased connectivity within primary information processing networks (e.g., SM and VI) of elderly subjects (Geerligs et al., 2015; Jockwitz et al., 2017). Interestingly, according to our results, these network-specific alterations do not seem to necessarily reflect the distinct accumulation of Abeta (Palmqvist et al., 2017) and tau proteins (Leuzy et al., 2022), but rather indicate more general aging-related changes.

5. Conclusion & limitations

In sum, we revealed substantial regional variations of explained CMRGlu by whole-brain BOLD FC input. The closely matching pattern of AG, synaptic density and signaling-related mRNA suggests that our model reflects interregional on-demand synaptic signaling fueled by anaerobic metabolism. However, mRNA maps were based on postmortem data from the Allen Human Brain Atlas, which might limit their applicability to individual neuroimaging data. Their limitation to neuro-related genes leaves aside other contributors to synaptic activity such as astrocytes. In addition, [^{11}C]UCB-J binds at presynaptic SV2A, and thus represents an estimate of general synaptic density. We further acknowledge that causal relationships between the observed findings from human brain imaging and the assumed physiological underpinnings of FSP+ to explain regional differences of modeled CMRGlu still need to be established. Our approach proved useful in further characterization of brain networks, which are usually metabolically underspecified. Future studies should investigate if the observed network optimization reveals formerly hidden networks and if a predictive processing account of the modeled input signals proves valid.

Concerning the aging brain, it needs to be acknowledged that data from the ADNI 2 cohort were acquired differently. This includes acquisition of rsfMRI and [^{18}F]FDG PET data sequentially and on different scanning days, with different acquisition parameters and without full quantification of CMRGlu. However, at least the latter aspect should not substantially affect the outcome of our study, since

MCM only uses the spatial pattern of the glucose metabolism (Godbersen et al., 2024). Future investigations should therefore apply homogenous acquisitions of simultaneous PET/MRI to optimize comparability across cohorts. Furthermore, even though the elderly cohort consisted of healthy subjects with mild atrophy, the reduction in brain volume might lead to an overestimated decrease in [^{18}F]FDG uptake when no PVC is applied (Greve et al., 2016). Still, the pronounced dedifferentiation of the explained metabolism indicates an altered interplay between functional interactions and energy demands in the aging brain, which might also prove fruitful for investigating psychiatric and neurodegenerative diseases. The interpretation of a regionally varying loss of FSP+ provides a testable hypothesis and a potential approach to assess therapeutic interventions to decelerate cognitive decline in pathological conditions that involve reduced cognitive flexibility like Alzheimer's disease, schizophrenia, or depression.

CRediT authorship contribution statement

Sebastian Klug: Writing – review & editing, Writing – original draft, Investigation, Formal analysis, Data curation. **Matej Murgaš:** Writing – review & editing, Writing – original draft, Formal analysis, Data curation. **Godber M Godbersen:** Writing – review & editing, Investigation. **Marcus Hacker:** Writing – review & editing, Resources, Methodology, Conceptualization. **Rupert Lanzenberger:** Writing – review & editing, Resources, Project administration, Methodology, Funding acquisition, Conceptualization. **Andreas Hahn:** Writing – review & editing, Writing – original draft, Resources, Project administration, Methodology, Investigation, Funding acquisition, Formal analysis, Data curation, Conceptualization.

Declaration of competing interest

R. Lanzenberger received investigator-initiated research funding from Siemens Healthcare regarding clinical research using PET/MR. He is a shareholder of the start-up company BM Health GmbH since 2019. M. Hacker received consulting fees and/or honoraria from Bayer Healthcare BMS, Eli Lilly, EZAG, GE Healthcare, Ipsen, ITM, Janssen, Roche, and Siemens Healthineers. All other authors report no conflict of interest in relation to this study.

Data availability

Raw data will not be publicly available due to reasons of data protection. Processed data and custom code can be obtained from the corresponding author with a data-sharing agreement, approved by the departments of legal affairs and data clearing of the Medical University of Vienna.

Acknowledgements

We are particularly grateful to Richard E. Carson for providing SV2A data as well as Manu Goyal and Andrei Vlassenko for providing OGI data. We thank the graduated team members and the diploma students of the Neuroimaging Lab (NIL, head: R. Lanzenberger) as well as the clinical colleagues from the Department of Psychiatry and Psychotherapy for clinical and/or administrative support. In detail, we would like to thank S. Kasper, K. Papageorgiou, P. Michenthaler, T. Vanicek, A. Basaran, M. Hienert, L. Silberbauer, J. Unterholzner and G. Gryglewski for medical support, L. Rischka, M. Klöbl and M. B. Reed for acquisition and analysis support, V. Ritter, K. Einenkel and E. Sittenberger for subject recruitment and A. Jelicic for partly implementation of the task. We are further grateful to W. Wadsak, V. Pichler, J. Raitanen, J. Völkle and A. Pomberger for radioligand synthesis. The scientific project was performed with the support of the Medical Imaging Cluster of the Medical University of Vienna. This research was funded in whole, or in part, by the Austrian Science Fund (FWF) [Grant DOI: 1055776/KLI610, PI: A. Hahn]. For open access purposes, the author has applied a CC BY public copyright license to any author accepted manuscript version arising from this submission. M. Murgaš was funded by the Austrian Science Fund (FWF) [Grant DOI:10.55776/DOC33, PI/Supervisor R. Lanzenberger]. S. Klug was supported by the MDPhD Excellence Program of the Medical University of Vienna. Data collection and sharing for this project was funded by the Alzheimer's Disease Neuroimaging Initiative (ADNI) (National Institutes of Health Grant U01 AG024904) and DOD ADNI (Department of Defense award number W81XWH-12-2-0012). ADNI is funded by the National Institute on Aging, the National Institute of Biomedical Imaging and Bioengineering, and through generous contributions from the following: AbbVie, Alzheimer's Association; Alzheimer's Drug Discovery Foundation; Araclon Biotech; BioClinica, Inc.; Biogen; Bristol-Myers Squibb Company; CereSpir, Inc.; Cogstate; Eisai Inc.; Elan Pharmaceuticals, Inc.; Eli Lilly and Company; EuroImmun; F. Hoffmann-La Roche Ltd and its affiliated company Genentech, Inc.; Fujirebio; GE Healthcare; IXICO Ltd.; Janssen Alzheimer Immunotherapy Research & Development, LLC.; Johnson & Johnson Pharmaceutical Research & Development LLC.; Lumosity; Lundbeck; Merck & Co., Inc.; Meso Scale Diagnostics, LLC.; NeuroRx Research; Neurotrack Technologies; Novartis Pharmaceuticals Corporation; Pfizer Inc.; Piramal Imaging; Servier; Takeda Pharmaceutical Company; and Transition Therapeutics. The Canadian Institutes of Health Research is providing funds to support ADNI clinical sites in Canada. Private sector contributions are facilitated by the Foundation for the National Institutes of Health (www.fnih.org). The grantee organization is the Northern California Institute for Research and Education, and the study is coordinated by the Alzheimer's Therapeutic Research Institute at the University of Southern California. ADNI data are disseminated by the Laboratory for Neuro Imaging at the University of Southern California.

Supplementary materials

Supplementary material associated with this article can be found, in the online version, at doi:10.1016/j.neuroimage.2024.120658.

References

Agren, T., Hoppe, J.M., Singh, L., Holmes, E.A., Rosén, J., 2021. The neural basis of Tetris gameplay: implicating the role of visuospatial processing. Curr. Psychol. https://doi.org/10.1007/s12144-021-02081-z.

Aiello, M., Salvatore, E., Cachia, A., Pappatà, S., Cavaliere, C., Prinster, A., Nicolai, E., Salvatore, M., Baron, J.-C., Quarantelli, M., 2015. Relationship between simultaneously acquired resting-state regional cerebral glucose metabolism and functional MRI: a PET/MR hybrid scanner study. Neuroimage 113, 111–121. https://doi.org/10.1016/j.neuroimage.2015.03.017.

Arnemann, K.L., Stöber, F., Narayan, S., Rabinovici, G.D., Jagust, W.J., 2017. Metabolic brain networks in aging and preclinical Alzheimer's disease. Neuroimage Clin. 17, 987–999. https://doi.org/10.1016/j.nicl.2017.12.037.

Ashburner, M., Lewis, S., 2002. On ontologies for biologists: the gene ontology–untangling the web. Novartis. Found. Symp. 247, 66–80 discussion 80-83, 84–90, 244–252.

Attwell, D., Buchan, A.M., Charpak, S., Lauritzen, M., MacVicar, B.A., Newman, E.A., 2010. Glial and neuronal control of brain blood flow. Nature 468, 232–243. https://doi.org/10.1038/nature09613.

Attwell, D., Laughlin, S.B., 2001. An energy budget for signaling in the grey matter of the brain. J. Cereb. Blood Flow Metab. 21, 1133–1145. https://doi.org/10.1097/00004647-200110000-00001.

Avena-Koenigsberger, A., Yan, X., Kolchinsky, A., Heuvel, M.P.van den, Hagmann, P., Sporns, O., 2019. A spectrum of routing strategies for brain networks. PLoS Comput. Biol. 15, e1006833 https://doi.org/10.1371/journal.pcbi.1006833.

Baldassarre, A., Lewis, C.M., Committeri, G., Snyder, A.Z., Romani, G.L., Corbetta, M., 2012. Individual variability in functional connectivity predicts performance of a perceptual task. Proc. Natl. Acad. Sci. U.S.A. 109, 3516–3521. https://doi.org/10.1073/pnas.1113148109.

Barron, H.C., Auksztulewicz, R., Friston, K., 2020. Prediction and memory: a predictive coding account. Prog. Neurobiol. 192, 101821 https://doi.org/10.1016/j.pneurobio.2020.101821.

Bijsterbosch, J.D., Beckmann, C.F., Woolrich, M.W., Smith, S.M., Harrison, S.J., 2019. The relationship between spatial configuration and functional connectivity of brain regions revisited. Elife 8, e44890. https://doi.org/10.7554/eLife.44890.

Blazey, T., Snyder, A.Z., Su, Y., Goyal, M.S., Lee, J.J., Vlassenko, A.G., Arbeláez, A.M., Raichle, M.E., 2019. Quantitative positron emission tomography reveals regional differences in aerobic glycolysis within the human brain. J. Cereb. Blood Flow Metab. 39, 2096–2102. https://doi.org/10.1177/0271678X18767005.

Brown, R.M., Gruijters, S.L.K., Kotz, S.A., 2022. Prediction in the aging brain: merging cognitive, neurological, and evolutionary perspectives. J. Gerontol.: Ser. B 77, 1580–1591. https://doi.org/10.1093/geronb/gbac062.

Buckner, R.L., DiNicola, L.M., 2019. The brain's default network: updated anatomy, physiology and evolving insights. Nat. Rev. Neurosci. 20, 593–608. https://doi.org/10.1038/s41583-019-0212-7.

Burgos, N., Cardoso, M.J., Thielemans, K., Modat, M., Pedemonte, S., Dickson, J., Barnes, A., Ahmed, R., Mahoney, C.J., Schott, J.M., Duncan, J.S., Atkinson, D., Arridge, S.R., Hutton, B.F., Ourselin, S., 2014. Attenuation correction synthesis for hybrid PET-MR scanners: application to brain studies. IEEE Trans. Med. Imaging 33, 2332–2341. https://doi.org/10.1109/TMI.2014.2340135.

Buzsáki, G., Wang, X.-J., 2012. Mechanisms of gamma oscillations. Annu Rev. Neurosci. 35, 203–225. https://doi.org/10.1146/annurev-neuro-062111-150444.

Carson, R.E., Naganawa, M., Toyonaga, T., Koohsari, S., Yang, Y., Chen, M.-K., Matuskey, D., Finnema, S.J., 2022. Imaging of synaptic density in neurodegenerative disorders. J. Nucl. Med. 63, 60S–67S. https://doi.org/10.2967/jnumed.121.263201.

Chan, J.S., Wibral, M., Stawowsky, C., Brandl, M., Helbling, S., Naumer, M.J., Kaiser, J., Wollstadt, P., 2021. Predictive coding over the lifespan: increased reliance on perceptual priors in older adults—a magnetoencephalography and dynamic causal modeling study. Front. Aging Neurosci. 13.

Chen, Y., Lin, Q., Liao, X., Zhou, C., He, Y., 2021. Association of aerobic glycolysis with the structural connectome reveals a benefit–risk balancing mechanism in the human brain. PNAS 118. https://doi.org/10.1073/pnas.2013232118.

Cohen, J.R., D'Esposito, M., 2016. The segregation and integration of distinct brain networks and their relationship to cognition. J. Neurosci. 36, 12083–12094. https://doi.org/10.1523/JNEUROSCI.2965-15.2016.

Cohen, J.R., Gallen, C.L., Jacobs, E.G., Lee, T.G., D'Esposito, M., 2014. Quantifying the reconfiguration of intrinsic networks during working memory. PLoS One 9, e106636. https://doi.org/10.1371/journal.pone.0106636.

Cole, M.W., Bassett, D.S., Power, J.D., Braver, T.S., Petersen, S.E., 2014. Intrinsic and task-evoked network architectures of the human brain. Neuron 83, 238–251. https://doi.org/10.1016/j.neuron.2014.05.014.

Cookson, S.L., D'Esposito, M., 2022. Evaluating the reliability, validity, and utility of overlapping networks: implications for network theories of cognition. Hum. Brain Mapp. hbm 26134. https://doi.org/10.1002/hbm.26134.

Craddock, R.C., James, G.A., Holtzheimer, P.E., Hu, X.P., Mayberg, H.S., 2012. A whole brain fMRI atlas generated via spatially constrained spectral clustering. Hum. Brain Mapp. 33, 1914–1928. https://doi.org/10.1002/hbm.21333.

Davis, S.W., Dennis, N.A., Daselaar, S.M., Fleck, M.S., Cabeza, R., 2008. Qué PASA? The posterior–anterior shift in aging. Cereb. Cortex 18, 1201–1209. https://doi.org/10.1093/cercor/bhm155.

Deco, G., Jirsa, V.K., McIntosh, A.R., 2011. Emerging concepts for the dynamical organization of resting-state activity in the brain. Nat. Rev. Neurosci. 12, 43–56. https://doi.org/10.1038/nrn2961.

Deery, H.A., Di Paolo, R., Moran, C., Egan, G.F., Jamadar, S.D., 2023a. Lower brain glucose metabolism in normal ageing is predominantly frontal and temporal: a systematic review and pooled effect size and activation likelihood estimates meta-analyses. Hum. Brain Mapp. 44, 1251–1277. https://doi.org/10.1002/hbm.26119.

Deery, H.A., Di Paolo, R., Moran, C., Egan, G.F., Jamadar, S.D., 2023b. The older adult brain is less modular, more integrated, and less efficient at rest: a systematic review of large-scale resting-state functional brain networks in aging. Psychophysiology 60, e14159. https://doi.org/10.1111/psyp.14159.

Dienel, G.A., 2019. Brain glucose metabolism: integration of energetics with function. Physiol. Rev. 99, 949–1045. https://doi.org/10.1152/physrev.00062.2017.

Diez, I., Sepulcre, J., 2018. Neurogenetic profiles delineate large-scale connectivity dynamics of the human brain. Nat. Commun. 9, 3876. https://doi.org/10.1038/s41467-018-06346-3.

DiNuzzo, M., Mangia, S., Moraschi, M., Mascali, D., Hagberg, G.E., Giove, F., 2022. Perception is associated with the brain's metabolic response to sensory stimulation. Elife 11, e71016. https://doi.org/10.7554/eLife.71016.

Farrell, M.E., Jiang, S., Schultz, A.P., Properzi, M.J., Price, J.C., Becker, J.A., Jacobs, H.I. L., Hanseeuw, B.J., Rentz, D.M., Villemagne, V.L., Papp, K.V., Mormino, E.C., Betensky, R.A., Johnson, K.A., Sperling, R.A., Buckley, R.F., 2021. Defining the lowest threshold for amyloid-PET to predict future cognitive decline and amyloid accumulation. Neurology 96. https://doi.org/10.1212/WNL.0000000000011214.

Finnema, S.J., Nabulsi, N.B., Eid, T., Detyniecki, K., Lin, S., Chen, M.-K., Dhaher, R., Matuskey, D., Baum, E., Holden, D., Spencer, D.D., Mercier, J., Hannestad, J., Huang, Y., Carson, R.E., 2016. Imaging synaptic density in the living human brain. Sci. Transl. Med. 8 https://doi.org/10.1126/scitranslmed.aaf6667.

Fischl, B., Salat, D.H., Busa, E., Albert, M., Dieterich, M., Haselgrove, C., van der Kouwe, A., Killiany, R., Kennedy, D., Klaveness, S., Montillo, A., Makris, N., Rosen, B., Dale, A.M., 2002. Whole brain segmentation: automated labeling of neuroanatomical structures in the human brain. Neuron 33, 341–355. https://doi.org/10.1016/s0896-6273(02)00569-x.

Fulcher, B.D., Arnatkeviciute, A., Fornito, A., 2021. Overcoming false-positive gene-category enrichment in the analysis of spatially resolved transcriptomic brain atlas data. Nat. Commun. 12, 2669. https://doi.org/10.1038/s41467-021-22862-1.

Gage, G.J., Stoetzner, C.R., Wiltschko, A.B., Berke, J.D., 2010. Selective activation of striatal fast-spiking interneurons during choice execution. Neuron 67, 466–479. https://doi.org/10.1016/j.neuron.2010.06.034.

Garrett, D.D., Kovacevic, N., McIntosh, A.R., Grady, C.L., 2011. The importance of being variable. J. Neurosci. 31, 4496–4503. https://doi.org/10.1523/JNEUROSCI.5641-10.2011.

Geerligs, L., Renken, R.J., Saliasi, E., Maurits, N.M., Lorist, M.M., 2015. A brain-wide study of age-related changes in functional connectivity. Cereb. Cortex 25, 1987–1999. https://doi.org/10.1093/cercor/bhu012.

The Gene Ontology Consortium, 2019. The gene ontology resource: 20 years and still GOing strong. Nucleic Acids Res. 47, D330–D338. https://doi.org/10.1093/nar/gky1055.

Genovese, C.R., Lazar, N.A., Nichols, T., 2002. Thresholding of statistical maps in functional neuroimaging using the false discovery rate. Neuroimage 15, 870–878. https://doi.org/10.1006/nimg.2001.1037.

Godbersen, G.M., Falb, P., Klug, S., Silberbauer, L.R., Reed, M.B., Nics, L., Hacker, M., Lanzenberger, R., Hahn, A., 2024. Non-invasive assessment of stimulation-specific changes in cerebral glucose metabolism with functional PET. Eur. J. Nucl. Med. Mol. Imaging. https://doi.org/10.1007/s00259-024-06675-0.

Godbersen, G.M., Klug, S., Wadsak, W., Pichler, V., Raitanen, J., Rieckmann, A., Stiernman, L., Cocchi, L., Breakspear, M., Hacker, M., Lanzenberger, R., Hahn, A., 2023. Task-evoked metabolic demands of the posteromedial default mode network are shaped by dorsal attention and frontoparietal control networks. Elife 12, e84683. https://doi.org/10.7554/eLife.84683.

Goyal, M.S., Blazey, T., Metcalf, N.V., McAvoy, M.P., Strain, J.F., Rahmani, M., Durbin, T.J., Xiong, C., Benzinger, T.L.-S., Morris, J.C., Raichle, M.E., Vlassenko, A. G., 2023. Brain aerobic glycolysis and resilience in Alzheimer disease. Proc. Natl. Acad. Sci. U.S.A. 120, e2212256120 https://doi.org/10.1073/pnas.2212256120.

Goyal, M.S., Hawrylycz, M., Miller, J.A., Snyder, A.Z., Raichle, M.E., 2014. Aerobic glycolysis in the human brain is associated with development and neotenous gene expression. Cell Metab. 19, 49–57. https://doi.org/10.1016/j.cmet.2013.11.020.

Goyal, M.S., Vlassenko, A.G., Blazey, T.M., Su, Y., Couture, L.E., Durbin, T.J., Bateman, R.J., Benzinger, T.L.-S., Morris, J.C., Raichle, M.E., 2017. Loss of brain aerobic glycolysis in normal human aging. Cell Metab. 26, 353–360. https://doi.org/10.1016/j.cmet.2017.07.010 e3.

Gratton, C., Laumann, T.O., Gordon, E.M., Adeyemo, B., Petersen, S.E., 2016. Evidence for two independent factors that modify brain networks to meet task goals. Cell Rep. 17, 1276–1288. https://doi.org/10.1016/j.celrep.2016.10.002.

Greve, D.N., Salat, D.H., Bowen, S.L., Izquierdo-Garcia, D., Schultz, A.P., Catana, C., Becker, J.A., Svarer, C., Knudsen, G.M., Sperling, R.A., Johnson, K.A., 2016. Different partial volume correction methods lead to different conclusions: an 18F-FDG-PET study of aging. Neuroimage 132, 334–343. https://doi.org/10.1016/j.neuroimage.2016.02.042.

Gryglewski, G., Seiger, R., James, G.M., Godbersen, G.M., Komorowski, A., Unterholzner, J., Michenthaler, P., Hahn, A., Wadsak, W., Mitterhauser, M., Kasper, S., Lanzenberger, R., 2018. Spatial analysis and high resolution mapping of the human whole-brain transcriptome for integrative analysis in neuroimaging. Neuroimage 176, 259–267. https://doi.org/10.1016/j.neuroimage.2018.04.068.

Guedj, E., Varrone, A., Boellaard, R., Albert, N.L., Barthel, H., van Berckel, B., Brendel, M., Cecchin, D., Ekmekcioglu, O., Garibotto, V., Lammertsma, A.A., Law, I., Peñuelas, I., Semah, F., Traub-Weidinger, T., van de Giessen, E., Van Weehaeghe, D., Morbelli, S., 2022. EANM procedure guidelines for brain PET imaging using [18F] FDG, version 3. Eur. J. Nucl. Med. Mol. Imaging 49, 632–651. https://doi.org/10.1007/s00259-021-05603-w.

Hahn, A., Breakspear, M., Rischka, L., Wadsak, W., Godbersen, G.M., Pichler, V., Michenthaler, P., Vanicek, T., Hacker, M., Kasper, S., Lanzenberger, R., Cocchi, L., 2020. Reconfiguration of functional brain networks and metabolic cost converge during task performance. ELife 9, e52443. https://doi.org/10.7554/eLife.52443.

Hahn, A., Gryglewski, G., Nics, L., Hienert, M., Rischka, L., Vraka, C., Sigurdardottir, H., Vanicek, T., James, G.M., Seiger, R., Kautzky, A., Silberbauer, L., Wadsak, W., Mitterhauser, M., Hacker, M., Kasper, S., Lanzenberger, R., 2016. Quantification of task-specific glucose metabolism with constant infusion of 18F-FDG. J. Nucl. Med. 57, 1933–1940. https://doi.org/10.2967/jnumed.116.176156.

Hahn, A., Gryglewski, G., Nics, L., Rischka, L., Ganger, S., Sigurdardottir, H., Vraka, C., Silberbauer, L., Vanicek, T., Kautzky, A., Wadsak, W., Mitterhauser, M., Hartenbach, M., Hacker, M., Kasper, S., Lanzenberger, R., 2018. Task-relevant brain networks identified with simultaneous PET/MR imaging of metabolism and connectivity. Brain Struct. Funct. 223, 1369–1378. https://doi.org/10.1007/s00429-017-1558-0.

Harris, J.J., Jolivet, R., Attwell, D., 2012. Synaptic energy use and supply. Neuron 75, 762–777. https://doi.org/10.1016/j.neuron.2012.08.019.

Hawrylycz, M.J., Lein, E.S., Guillozet-Bongaarts, A.L., Shen, E.H., Ng, L., Miller, J.A., van de Lagemaat, L.N., Smith, K.A., Ebbert, A., Riley, Z.L., Abajian, C., Beckmann, C.F., Bernard, A., Bertagnolli, D., Boe, A.F., Cartagena, P.M., Chakravarty, M.M., Chapin, M., Chong, J., Dalley, R.A., Daly, B.D., Dang, C., Datta, S., Dee, N., Dolbeare, T.A., Faber, V., Feng, D., Fowler, D.R., Goldy, J., Gregor, B.W., Haradon, Z., Haynor, D.R., Hohmann, J.G., Horvath, S., Howard, R.E., Jeromin, A., Jochim, J.M., Kinnunen, M., Lau, C., Lazarz, E.T., Lee, C., Lemon, T.A., Li, L., Li, Y., Morris, J.A., Overly, C.C., Parker, P.D., Parry, S.E., Reding, M., Royall, J.J., Schulkin, J., Sequeira, P.A., Slaughterbeck, C.R., Smith, S.C., Sodt, A.J., Sunkin, S. M., Swanson, B.E., Vawter, M.P., Williams, D., Wohnoutka, P., Zielke, H.R., Geschwind, D.H., Hof, P.R., Smith, S.M., Koch, C., Grant, S.G.N., Jones, A.R., 2012. An anatomically comprehensive atlas of the adult human brain transcriptome. Nature 489, 391–399. https://doi.org/10.1038/nature11405.

Hearne, L.J., Cocchi, L., Zalesky, A., Mattingley, J.B., 2017. Reconfiguration of brain network architectures between resting-state and complexity-dependent cognitive reasoning. J. Neurosci. 37, 8399–8411. https://doi.org/10.1523/JNEUROSCI.0485-17.2017.

Hertäg, L., Clopath, C., 2022. Prediction-error neurons in circuits with multiple neuron types: formation, refinement, and functional implications. Proc. Natl. Acad. Sci. U.S. A. 119, e2115699119 https://doi.org/10.1073/pnas.2115699119.
Hertäg, L., Sprekeler, H., 2020. Learning prediction error neurons in a canonical interneuron circuit. Elife 9, e57541. https://doi.org/10.7554/eLife.57541.
Hillman, E.M.C., 2014. Coupling mechanism and significance of the BOLD signal: a status report. Annu Rev. Neurosci. 37, 161–181. https://doi.org/10.1146/annurev-neuro-071013-014111.
Holmes, A.P., Blair, R.C., Watson, J.D., Ford, I., 1996. Nonparametric analysis of statistic images from functional mapping experiments. J. Cereb. Blood Flow Metab. 16, 7–22. https://doi.org/10.1097/00004647-199601000-00002.
Homayoun, H., Moghaddam, B., 2007. NMDA receptor hypofunction produces opposite effects on prefrontal cortex interneurons and pyramidal neurons. J. Neurosci. 27, 11496–11500. https://doi.org/10.1523/JNEUROSCI.2213-07.2007.
Howarth, C., Gleeson, P., Attwell, D., 2012. Updated energy budgets for neural computation in the neocortex and cerebellum. J. Cereb. Blood Flow Metab. 32, 1222–1232. https://doi.org/10.1038/jcbfm.2012.35.
Howarth, C., Peppiatt-Wildman, C.M., Attwell, D., 2010. The energy use associated with neural computation in the cerebellum. J. Cereb. Blood Flow Metab. 30, 403–414. https://doi.org/10.1038/jcbfm.2009.231.
Hsu, Y.-F., Waszak, F., Strömmer, J., Hämäläinen, J.A., 2021. Human brain ages with hierarchy-selective attenuation of prediction errors. Cereb. Cortex 31, 2156–2168. https://doi.org/10.1093/cercor/bhaa352.
Ito, T., Kulkarni, K.R., Schultz, D.H., Mill, R.D., Chen, R.H., Solomyak, L.I., Cole, M.W., 2017. Cognitive task information is transferred between brain regions via resting-state network topology. Nat. Commun. 8 https://doi.org/10.1038/s41467-017-01000-w.
Jamadar, S.D., Ward, P.G.D., Li, S., Sforazzini, F., Baran, J., Chen, Z., Egan, G.F., 2019. Simultaneous task-based BOLD-fMRI and [18-F] FDG functional PET for measurement of neuronal metabolism in the human visual cortex. Neuroimage 189, 258–266. https://doi.org/10.1016/j.neuroimage.2019.01.003.
Jockwitz, C., Caspers, S., Lux, S., Eickhoff, S.B., Jütten, K., Lenzen, S., Moebus, S., Pundt, N., Reid, A., Hoffstaedter, F., Jöckel, K.-H., Erbel, R., Cichon, S., Nöthen, M. M., Shah, N.J., Zilles, K., Amunts, K., 2017. Influence of age and cognitive performance on resting-state brain networks of older adults in a population-based cohort. Cortex 89, 28–44. https://doi.org/10.1016/j.cortex.2017.01.008.
Katsumi, Y., Theriault, J.E., Quigley, K.S., Barrett, L.F., 2022. Allostasis as a core feature of hierarchical gradients in the human brain. Network Neurosci. 6, 1010–1031. https://doi.org/10.1162/netn_a_00240.
Klein, A., Tourville, J., 2012. 101 Labeled brain images and a consistent human cortical labeling protocol. Front. Neurosci. 6 https://doi.org/10.3389/fnins.2012.00171.
Klug, S., Godbersen, G.M., Rischka, L., Wadsak, W., Pichler, V., Klöbl, M., Hacker, M., Lanzenberger, R., Hahn, A., 2022. Learning induces coordinated neuronal plasticity of metabolic demands and functional brain networks. Commun. Biol. 5, 1–12. https://doi.org/10.1038/s42003-022-03362-4.
Komorowski, A., Murgaš, M., Vidal, R., Singh, A., Gryglewski, G., Kasper, S., Wiltfang, J., Lanzenberger, R., Goya-Maldonado, R., 2022. Regional gene expression patterns are associated with task-specific brain activation during reward and emotion processing measured with functional MRI. Hum. Brain Mapp. 43, 5266–5280. https://doi.org/10.1002/hbm.26001.
Kooijmans, R.N., Self, M.W., Wouterlood, F.G., Beliën, J.A.M., Roelfsema, P.R., 2014. Inhibitory interneuron classes express complementary AMPA-receptor patterns in macaque primary visual cortex. J. Neurosci. 34, 6303–6315. https://doi.org/10.1523/JNEUROSCI.3188-13.2014.
Koush, Y., De Graaf, R.A., Kupers, R., Dricot, L., Ptito, M., Behar, K.L., Rothman, D.L., Hyder, F., 2021. Metabolic underpinnings of activated and deactivated cortical areas in human brain. J. Cereb. Blood Flow Metab. 41, 986–1000. https://doi.org/10.1177/0271678X21989186.
Krienen, F.M., Yeo, B.T.T., Buckner, R.L., 2014. Reconfigurable task-dependent functional coupling modes cluster around a core functional architecture. Philos. Trans. R. Soc. B: Biol. Sci. 369, 20130526 https://doi.org/10.1098/rstb.2013.0526.
Lee, K., Holley, S.M., Shobe, J.L., Chong, N.C., Cepeda, C., Levine, M.S., Masmanidis, S. C., 2017. Parvalbumin interneurons modulate striatal output and enhance performance during associative learning. Neuron 93. https://doi.org/10.1016/j.neuron.2017.02.033, 1451-1463.e4.
Leuzy, A., Smith, R., Cullen, N.C., Strandberg, O., Vogel, J.W., Binette, A.P., Borroni, E., Janelidze, S., Ohlsson, T., Jögi, J., Ossenkoppele, R., Palmqvist, S., Mattsson-Carlgren, N., Klein, G., Stomrud, E., Hansson, O., 2022. Biomarker-based prediction of longitudinal tau positron emission tomography in Alzheimer disease. JAMA Neurol. 79, 149–158. https://doi.org/10.1001/jamaneurol.2021.4654.
Leybaert, L., 2005. Neurobarrier coupling in the brain: a partner of neurovascular and neurometabolic coupling? J. Cereb. Blood Flow Metab. 25, 2–16. https://doi.org/10.1038/sj.jcbfm.9600001.
Logothetis, N.K., 2008. What we can do and what we cannot do with fMRI. Nature 453, 869–878. https://doi.org/10.1038/nature06976.
Lundgaard, I., Li, B., Xie, L., Kang, H., Sanggaard, S., Haswell, J.D.R., Sun, W., Goldman, S., Blekot, S., Nielsen, M., Takano, T., Deane, R., Nedergaard, M., 2015. Direct neuronal glucose uptake heralds activity-dependent increases in cerebral metabolism. Nat. Commun. 6, 6807. https://doi.org/10.1038/ncomms7807.
Magistretti, P.J., Allaman, I., 2015. A cellular perspective on brain energy metabolism and functional imaging. Neuron 86, 883–901. https://doi.org/10.1016/j.neuron.2015.03.035.
Margulies, D.S., Ghosh, S.S., Goulas, A., Falkiewicz, M., Huntenburg, J.M., Langs, G., Bezgin, G., Eickhoff, S.B., Castellanos, F.X., Petrides, M., Jefferies, E., Smallwood, J., 2016. Situating the default-mode network along a principal gradient of macroscale cortical organization. Proc. Natl. Acad. Sci. U.S.A. 113, 12574–12579. https://doi.org/10.1073/pnas.1608282113.
Martins, D., Giacomel, A., Williams, S.C.R., Turkheimer, F., Dipasquale, O., Veronese, M., 2021. Imaging transcriptomics: convergent cellular, transcriptomic, and molecular neuroimaging signatures in the healthy adult human brain. Cell Rep. 37, 110173 https://doi.org/10.1016/j.celrep.2021.110173.
Mattar, M.G., Cole, M.W., Thompson-Schill, S.L., Bassett, D.S., 2015. A functional cartography of cognitive systems. PLoS Comput. Biol. 11, e1004533 https://doi.org/10.1371/journal.pcbi.1004533.
Mergenthaler, P., Lindauer, U., Dienel, G.A., Meisel, A., 2013. Sugar for the brain: the role of glucose in physiological and pathological brain function. Trends Neurosci. 36, 587–597. https://doi.org/10.1016/j.tins.2013.07.001.
Mishra, A., Reynolds, J.P., Chen, Y., Gourine, A.V., Rusakov, D.A., Attwell, D., 2016. Astrocytes mediate neurovascular signaling to capillary pericytes but not to arterioles. Nat. Neurosci. 19, 1619–1627. https://doi.org/10.1038/nn.4428.
Mormino, E.C., 2014. Amyloid and APOE e4 interact to influence short-term decline in preclinical Alzheimer disease.
Murphy, K., Fox, M.D., 2017. Towards a consensus regarding global signal regression for resting state functional connectivity MRI. Neuroimage 154, 169–173. https://doi.org/10.1016/j.neuroimage.2016.11.052.
Nørgaard, M., Beliveau, V., Ganz, M., Svarer, C., Pinborg, L.H., Keller, S.H., Jensen, P.S., Greve, D.N., Knudsen, G.M., 2021. A high-resolution in vivo atlas of the human brain's benzodiazepine binding site of GABAA receptors. Neuroimage 232, 117878. https://doi.org/10.1016/j.neuroimage.2021.117878.
Nugent, A.C., Martinez, A., D'Alfonso, A., Zarate, C.A., Theodore, W.H., 2015. The relationship between glucose metabolism, resting-state fMRI BOLD signal, and GABAA-binding potential: a preliminary study in healthy subjects and those with temporal lobe epilepsy. J. Cereb. Blood Flow Metab. 35, 583–591. https://doi.org/10.1038/jcbfm.2014.228.
Onwordi, E.C., Whitehurst, T., Mansur, A., Statton, B., Berry, A., Quinlan, M., O'Regan, D.P., Rogdaki, M., Marques, T.R., Rabiner, E.A., Gunn, R.N., Vernon, A.C., Natesan, S., Howes, O.D., 2021. The relationship between synaptic density marker SV2A, glutamate and N-acetyl aspartate levels in healthy volunteers and schizophrenia: a multimodal PET and magnetic resonance spectroscopy brain imaging study. Transl. Psychiatry 11, 1–9. https://doi.org/10.1038/s41398-021-01515-3.
Palmqvist, S., Schöll, M., Strandberg, O., Mattsson, N., Stomrud, E., Zetterberg, H., Blennow, K., Landau, S., Jagust, W., Hansson, O., 2017. Earliest accumulation of β-amyloid occurs within the default-mode network and concurrently affects brain connectivity. Nat. Commun. 8, 1214. https://doi.org/10.1038/s41467-017-01150-x.
Palombit, A., Silvestri, E., Volpi, T., Aiello, M., Cecchin, D., Bertoldo, A., Corbetta, M., 2022. Variability of regional glucose metabolism and the topology of functional networks in the human brain. Neuroimage 257, 119280. https://doi.org/10.1016/j.neuroimage.2022.119280.
Palop, J.J., Mucke, L., 2016. Network abnormalities and interneuron dysfunction in Alzheimer disease. Nat. Rev. Neurosci. 17, 777–792. https://doi.org/10.1038/nrn.2016.141.
Power, J.D., Schlaggar, B.L., Petersen, S.E., 2015. Recent progress and outstanding issues in motion correction in resting state fMRI. Neuroimage 0, 536–551. https://doi.org/10.1016/j.neuroimage.2014.10.044.
Raichle, M.E., 2015. The restless brain: how intrinsic activity organizes brain function. Philos. Trans. R. Soc. B: Biol. Sci. 370, 20140172 https://doi.org/10.1098/rstb.2014.0172.
Raichle, M.E., 2010. Two views of brain function. Trends. Cogn. Sci. 14, 180–190. https://doi.org/10.1016/j.tics.2010.01.008.
Raichle, M.E., Mintun, M.A., 2006. Brain work and brain imaging. Annu Rev. Neurosci. 29, 449–476. https://doi.org/10.1146/annurev.neuro.29.051605.112819.
Rajkumar, R., Régio Brambilla, C., Veselinović, T., Bierbrier, J., Wyss, C., Ramkiran, S., Orth, L., Lang, M., Rota Kops, E., Mauler, J., Scheins, J., Neumaier, B., Ermert, J., Herzog, H., Langen, K.-J., Binkofski, F.C., Lerche, C., Shah, N.J., Neuner, I., 2021. Excitatory–inhibitory balance within EEG microstates and resting-state fMRI networks: assessed via simultaneous trimodal PET–MR–EEG imaging. Transl. Psychiatry 11, 1–15. https://doi.org/10.1038/s41398-020-01160-2.
Riedl, V., Bienkowska, K., Strobel, C., Tahmasian, M., Grimmer, T., Förster, S., Friston, K. J., Sorg, C., Drzezga, A., 2014. Local activity determines functional connectivity in the resting human brain: a simultaneous FDG-PET/fMRI study. J. Neurosci. 34, 6260–6266. https://doi.org/10.1523/JNEUROSCI.0492-14.2014.
Riedl, V., Utz, L., Castrillón, G., Grimmer, T., Rauschecker, J.P., Ploner, M., Friston, K.J., Drzezga, A., Sorg, C., 2016. Metabolic connectivity mapping reveals effective connectivity in the resting human brain. Proc. Natl. Acad. Sci. U.S.A. 113, 428–433. https://doi.org/10.1073/pnas.1513752113.
Rischka, L., Godbersen, G.M., Pichler, V., Michenthaler, P., Klug, S., Klöbl, M., Ritter, V., Wadsak, W., Hacker, M., Kasper, S., Lanzenberger, R., Hahn, A., 2021. Reliability of task-specific neuronal activation assessed with functional PET, ASL and BOLD imaging. J. Cereb. Blood Flow Metab. https://doi.org/10.1177/0271678X211020589, 0271678×211020589.
Rischka, L., Gryglewski, G., Pfaff, S., Vanicek, T., Hienert, M., Klöbl, M., Hartenbach, M., Haug, A., Wadsak, W., Mitterhauser, M., Hacker, M., Kasper, S., Lanzenberger, R., Hahn, A., 2018. Reduced task durations in functional PET imaging with [18F]FDG approaching that of functional MRI. Neuroimage 181, 323–330. https://doi.org/10.1016/j.neuroimage.2018.06.079.
Rossano, S., Toyonaga, T., Finnema, S.J., Naganawa, M., Lu, Y., Nabulsi, N., Ropchan, J., De Bruyn, S., Otoul, C., Stockis, A., Nicolas, J.-M., Martin, P., Mercier, J., Huang, Y., Maguire, R.P., Carson, R.E., 2020. Assessment of a white matter reference region for ^{11}C-UCB-J PET quantification. J. Cereb. Blood Flow Metab. 40, 1890–1901. https://doi.org/10.1177/0271678X19879230.

Roux, L., Buzsáki, G., 2015. Tasks for inhibitory interneurons in intact brain circuits. Neuropharmacology 0, 10–23. https://doi.org/10.1016/j.neuropharm.2014.09.011.
Schaefer, A., Kong, R., Gordon, E.M., Laumann, T.O., Zuo, X.-N., Holmes, A.J., Eickhoff, S.B., Yeo, B.T.T., 2018. Local-global parcellation of the human cerebral cortex from intrinsic functional connectivity MRI. Cereb. Cortex 28, 3095–3114. https://doi.org/10.1093/cercor/bhx179.
Schultz, D.H., Cole, M.W., 2016. Integrated brain network architecture supports cognitive task performance. Neuron 92, 278–279. https://doi.org/10.1016/j.neuron.2016.10.004.
Seguin, C., Razi, A., Zalesky, A., 2019. Inferring neural signalling directionality from undirected structural connectomes. Nat. Commun. 10, 4289. https://doi.org/10.1038/s41467-019-12201-w.
Shannon, B.J., Vaishnavi, S.N., Vlassenko, A.G., Shimony, J.S., Rutlin, J., Raichle, M.E., 2016. Brain aerobic glycolysis and motor adaptation learning. PNAS 113, E3782–E3791. https://doi.org/10.1073/pnas.1604977113.
Shen, E.H., Overly, C.C., Jones, A.R., 2012a. The Allen Human Brain Atlas: comprehensive gene expression mapping of the human brain. Trends. Neurosci. 35, 711–714. https://doi.org/10.1016/j.tins.2012.09.005.
Shen, X., Liu, H., Hu, Z., Hu, H., Shi, P., 2012b. The relationship between cerebral glucose metabolism and age: report of a large brain PET data set. PLoS One 7, e51517. https://doi.org/10.1371/journal.pone.0051517.
Sheth, B.R., Young, R., 2016. Two visual pathways in primates based on sampling of space: exploitation and exploration of visual information. Front. Integr. Neurosci. 10, 37. https://doi.org/10.3389/fnint.2016.00037.
Shine, J.M., Bissett, P.G., Bell, P.T., Koyejo, O., Balsters, J.H., Gorgolewski, K.J., Moodie, C.A., Poldrack, R.A., 2016. The dynamics of functional brain networks: integrated network states during cognitive task performance. Neuron 92, 544–554. https://doi.org/10.1016/j.neuron.2016.09.018.
Shokri-Kojori, E., Tomasi, D., Alipanahi, B., Wiers, C.E., Wang, G.-J., Volkow, N.D., 2019. Correspondence between cerebral glucose metabolism and BOLD reveals relative power and cost in human brain. Nat. Commun. 10, 690. https://doi.org/10.1038/s41467-019-08546-x.
Smallwood, J., Bernhardt, B.C., Leech, R., Bzdok, D., Jefferies, E., Margulies, D.S., 2021. The default mode network in cognition: a topographical perspective. Nat. Rev. Neurosci. 22, 503–513. https://doi.org/10.1038/s41583-021-00474-4.
Sokoloff, L., 1981. Relationships among local functional activity, energy metabolism, and blood flow in the central nervous system. Fed. Proc. 40, 2311–2316.
Sokoloff, L., Reivich, M., Kennedy, C., Des Rosiers, M.H., Patlak, C.S., Pettigrew, K.D., Sakurada, O., Shinohara, M., 1977. The [14C]deoxyglucose method for the measurement of local cerebral glucose utilization: theory, procedure, and normal values in the conscious and anesthetized albino rat. J. Neurochem. 28, 897–916.
Spadone, S., Della Penna, S., Sestieri, C., Betti, V., Tosoni, A., Perrucci, M.G., Romani, G. L., Corbetta, M., 2015. Dynamic reorganization of human resting-state networks during visuospatial attention. Proc. Natl. Acad. Sci. 112, 8112–8117. https://doi.org/10.1073/pnas.1415439112.
Spreng, R.N., Turner, G.R., 2019. The shifting architecture of cognition and brain function in older adulthood. Perspect. Psychol. Sci. 14, 523–542. https://doi.org/10.1177/1745691619827511.
Stiernman, L.J., Grill, F., Hahn, A., Rischka, L., Lanzenberger, R., Lundmark, V.P., Riklund, K., Axelsson, J., Rieckmann, A., 2021. Dissociations between glucose metabolism and blood oxygenation in the human default mode network revealed by simultaneous PET-fMRI. PNAS 118. https://doi.org/10.1073/pnas.2021913118.
Sun, F.T., Miller, L.M., D'Esposito, M., 2004. Measuring interregional functional connectivity using coherence and partial coherence analyses of fMRI data. Neuroimage 21, 647–658. https://doi.org/10.1016/j.neuroimage.2003.09.056.
Theriault, J., Shaffer, C., Dienel, G.A., Sander, C.Y., Hooker, J.M., Dickerson, B.C., Barrett, L.F., Quigley, K., 2021. Aerobic glycolysis, the efficiency tradeoff hypothesis, and the biological basis of neuroimaging: a solution to a metabolic mystery at the heart of neuroscience. doi:10.31234/osf.io/pkzr8.
Yeo, B.T.T., Krienen, F.M., Sepulcre, J., Sabuncu, M.R., Lashkari, D., Hollinshead, M., Roffman, J.L., Smoller, J.W., Zöllei, L., Polimeni, J.R., Fischl, B., Liu, H., Buckner, R. L., 2011. The organization of the human cerebral cortex estimated by intrinsic functional connectivity. J. Neurophysiol. 106, 1125–1165. https://doi.org/10.1152/jn.00338.2011.
Tomasi, D., Wang, G.-J., Volkow, N.D., 2013. Energetic cost of brain functional connectivity. Proc. Natl. Acad. Sci. U.S.A. 110, 13642–13647. https://doi.org/10.1073/pnas.1303346110.
Tomasi, D.G., Shokri-Kojori, E., Wiers, C.E., Kim, S.W., Demiral, Ş.B., Cabrera, E.A., Lindgren, E., Miller, G., Wang, G.-J., Volkow, N.D., 2017. Dynamic brain glucose metabolism identifies anti-correlated cortical-cerebellar networks at rest. J. Cereb. Blood Flow Metab. 37, 3659–3670. https://doi.org/10.1177/0271678X17708692.
Turner, G.R., Spreng, R.N., 2015. Prefrontal engagement and reduced default network suppression co-occur and are dynamically coupled in older adults: the default–executive coupling hypothesis of aging. J. Cogn. Neurosci. 27, 2462–2476. https://doi.org/10.1162/jocn_a_00869.
Vaishnavi, S.N., Vlassenko, A.G., Rundle, M.M., Snyder, A.Z., Mintun, M.A., Raichle, M. E., 2010. Regional aerobic glycolysis in the human brain. Proc. Natl. Acad. Sci. USA 107, 17757–17762. https://doi.org/10.1073/pnas.1010459107.
van Aalst, J., Ceccarini, J., Sunaert, S., Dupont, P., Koole, M., Van Laere, K., 2021. In vivo synaptic density relates to glucose metabolism at rest in healthy subjects, but is strongly modulated by regional differences. J. Cereb. Blood Flow Metab. 41, 1978–1987. https://doi.org/10.1177/0271678X20981502.
van den Heuvel, M.P., Scholtens, L.H., Turk, E., Mantini, D., Vanduffel, W., Feldman Barrett, L., 2016. Multimodal analysis of cortical chemoarchitecture and macroscale fMRI resting-state functional connectivity. Hum. Brain Mapp. 37, 3103–3113. https://doi.org/10.1002/hbm.23229.
Villien, M., Wey, H.-Y., Mandeville, J.B., Catana, C., Polimeni, J.R., Sander, C.Y., Zürcher, N.R., Chonde, D.B., Fowler, J.S., Rosen, B.R., Hooker, J.M., 2014. Dynamic functional imaging of brain glucose utilization using fPET-FDG. Neuroimage 100, 192–199. https://doi.org/10.1016/j.neuroimage.2014.06.025.
Vlassenko, A.G., Vaishnavi, S.N., Couture, L., Sacco, D., Shannon, B.J., Mach, R.H., Morris, J.C., Raichle, M.E., Mintun, M.A., 2010. Spatial correlation between brain aerobic glycolysis and amyloid-β (Aβ) deposition. Proc. Natl. Acad. Sci. U.S.A. 107, 17763–17767. https://doi.org/10.1073/pnas.1010461107.
Volpi, T., Silvestri, E., Aiello, M., Corbetta, M., Bertoldo, A., 2021. The complexity of the relationship between spontaneous brain activity and glucose metabolism (preprint). In Review. doi:10.21203/rs.3.rs-728300/v1.
Westphal, A.J., Wang, S., Rissman, J., 2017. Episodic memory retrieval benefits from a less modular brain network organization. J. Neurosci. 37, 3523–3531. https://doi.org/10.1523/JNEUROSCI.2509-16.2017.
Wig, G.S., 2017. Segregated systems of human brain networks. Trends. Cogn. Sci. 21, 981–996. https://doi.org/10.1016/j.tics.2017.09.006.
Yau, J.O.-Y., Chaichim, C., Power, J.M., McNally, G.P., 2021. The roles of basolateral amygdala parvalbumin neurons in fear learning. J. Neurosci. 41, 9223–9234. https://doi.org/10.1523/JNEUROSCI.2461-20.2021.
Yeo, B.T.T., Krienen, F.M., Eickhoff, S.B., Yaakub, S.N., Fox, P.T., Buckner, R.L., Asplund, C.L., Chee, M.W.L., 2016. Functional specialization and flexibility in human association cortex. Cereb. Cortex 26, 465. https://doi.org/10.1093/cercor/bhv260.
Yu, X., 2022. Less is more: a critical role of synapse pruning in neural circuit wiring. Nat. Rev. Neurosci. 1–1 https://doi.org/10.1038/s41583-022-00665-7.
Yu, Y., Herman, P., Rothman, D.L., Agarwal, D., Hyder, F., 2018. Evaluating the gray and white matter energy budgets of human brain function. J. Cereb. Blood Flow Metab. 38, 1339–1353. https://doi.org/10.1177/0271678X17708691.
Zimmer, E.R., Parent, M.J., Souza, D.G., Leuzy, A., Lecrux, C., Kim, H.-I., Gauthier, S., Pellerin, L., Hamel, E., Rosa-Neto, P., 2017. [18F]FDG PET signal is driven by astroglial glutamate transport. Nat. Neurosci. 20, 393–395. https://doi.org/10.1038/nn.4492.